MASARYKOVA UNIVERZITA

Přírodovědecká fakulta

Ústav teoretické fyziky a astrofyziky

Bakalářská práce

Brno 2024 **Filip Holoubek**

MASARYKOVA UNIVERZITA

Přírodovědecká fakulta

Ústav teoretické fyziky a astrofyziky

Bakalářská práce

Superzářivé supernovy

Filip Holoubek

Vedoucí práce: Mgr. Ing. arch. Petr Kurfürst, Ph.D.

Brno 2024

Bibliografický záznam

Autor:	Filip Holoubek Přírodovědecká fakulta, Masarykova univerzita Ústav teoretické fyziky a astrofyziky
Název práce:	Superzářivé supernovy
Studijní program:	Fyzika
Studijní plán:	Astrofyzika
Vedoucí práce:	Mgr. Ing. arch. Petr Kurfürst, Ph.D.
Akademický rok:	2023/2024
Počet stran:	X + 48
Klíčová slova:	Supernovy, interakce s CSM, hydrodynamika, světelné křivky, spektra, SNEC, CASTRO, SEDONA

Bibliographic entry

Author:	Filip Holoubek Faculty of Science, Masaryk University Department of Theoretical Physics and Astrophysics
Title of Thesis:	Superluminous supernovae
Degree Programme:	Physics
Field of Study:	Astrophysics
Supervisor:	Mgr. Ing. arch. Petr Kurfürst, Ph.D.
Academic year:	2023/2024
Number of Pages:	X + 48
Keywords:	Supernovae, interactions with CSM, hydrodynamics, light curves, spectra, SNEC, CASTRO, SEDONA

Abstrakt

Superzářivé supernovy jsou unikátní děje, při kterých mohou vznikat extrémně jasné a dlouhotrvající světelné křivky, díky účinné interakci s okolní hvězdnou hmotou (CSM), i přes to, že původní energie exploze nemusí být zvlášť výrazná. Supernovy interagující s CSM mohou zobrazovat strukturu a množství mezihvězdné hmoty uvnitř mladých galaxií, ve kterých vznikají nové hvězdy. Jsou zkoumány dvě situace pro CSM – ekvatoriální disk a bipolární laloky vytvářející strukturu podobnou mlhovině Homunculus. Pomocí propojení více výpočetních kódů je možný detailnější pohled na jejich vývoj a interakce s CSM, ale také určit jejich světelné křivky a spektra. Pro simulování hydrodynamického vývoje a tvorbu modelů bylo využito propojení programů SNEC a CASTRO a pro získání světelných křivek a několika spekter v různých časech expanze byla jako vstupní data do programu Sedona využita data z CASTRO.

Abstract

Superluminous supernovae are unique events that can produce extremely bright and long-lasting light curves due to effective interaction with the surrounding circumstellar matter (CSM), even though the initial energy of the explosion may not be particularly significant. Supernovae interacting with the CSM can reveal the structure and abundance of interstellar matter in young galaxies where new stars are forming. Two situations for CSMs are investigated - an equatorial disk and bipolar lobes resembling in principle the Homunculus-like nebula. By linking several computational codes, a more detailed view of their evolution and interactions with the CSM is obtained, as well as the determination of their light curves and spectra. Linking SNEC and CASTRO was used to simulate the hydrodynamic models, and CASTRO data were used as input to SEDONA to obtain the light curves and spectra in several times of SN expansion.

MASARYKOVA UNIVERZITA
PŘÍRODOVĚDECKÁ FAKULTA
KOTLÁŘSKÁ 2, 611 37 BRNO
IČ: 00216224
DIČ: CZ00216224

ZADÁNÍ BAKALÁŘSKÉ PRÁCE

Akademický rok: 2023/2024

Ústav:	Ústav teoretické fyziky a astrofyziky
Student:	Filip Holoubek
Program:	Fyzika
Specializace:	Astrofyzika

Ředitel *ústavu* PřF MU Vám ve smyslu Studijního a zkušebního řádu MU určuje bakalářskou práci s názvem:

Název práce:	Superzářivé supernovy
Název práce anglicky:	Superluminous supernovae
Jazyk závěrečné práce:	angličtina

Oficiální zadání:
Důvodem, proč jsou tyto supernovy mimořádně zajímavé, je to, že interakce supernovy s okolním médiem je velmi účinným zdrojem extrémně jasných a dlouhotrvajících světelných křivek, i když původní energie exploze není nijak výjimečná. Dokonce umožňuje vznik velmi zářivých jevů i z explozí s poměrně nízkou energií nebo s nízkým podílem radioaktivity. V rámci bakalářské práce spočítáme semianalatickým způsobem i jednoduchým výpočetním programem světelné křivky, které mohou vznikat takovou interakcí, za předpokladu více či méně hustého okolního prostředí a výsledky potom budeme diskutovat s ohledem na skutečně pozorované světelné křivky supernov. Po dohodě se zájemcem může být jazykem práce angličtina.

Literatura:
KURFÜRST, Petr, Ondřej PEJCHA a Jiří KRTIČKA. Interaction of expanding supernova envelope with asymmetric circumstellar environment. In *The 35th Jerusalem Winter School in Theoretical Physics, December 27 - January 5, 2018, Jerusalem, ISRAEL*. 2017.

KURFÜRST, Petr a Jiří KRTIČKA. Modeling of interactions between supernovae ejecta and aspherical circumstellar environments. *Astronomy and Astrophysics*. Les Ulis: EDP SCIENCES S A, 2019, roč. 625, A24, s. 1-16. ISSN 1432-0746. Dostupné z: https://dx.doi.org/10.1051/0004-6361/201833429.

BRANCH, David a J. Craig WHEELER. *Supernova explosions*. Berlin, Germany: Springer, 2017, xix, 721. ISBN 9783662550526.

KURFÜRST, Petr, Ondřej PEJCHA a Jiří KRTIČKA. Supernova explosions interacting with aspherical circumstellar material: implications for light curves, spectral line profiles, and polarization. *Astronomy and Astrophysics*. Les Ulis: EDP Sciences, 2020, roč. 642, October 2020, s. 1-20. ISSN 0004-6361. Dostupné z: https://dx.doi.org/10.1051/0004-6361/202039073.

Vedoucí práce:	Mgr. Ing. arch. Petr Kurfürst, Ph.D.
Datum zadání práce:	5. 4. 2023
V Brně dne:	29. 4. 2024

Filip Holoubek, 17. 11. 2023
Mgr. Ing. arch. Petr Kurfürst, Ph.D., 21. 11. 2023
RNDr. Luboš Poláček, 5. 12. 2023

Poděkování

Na prvním místě bych chtěl poděkovat svému vedoucímu Mgr. Ing. arch. Petru Kurfürstovi, Ph.D. za mnoho trpělivosti a předání velkého množství znalostí a zkušeností ke studovanému tématu. Jako dalšímu bych chtěl poděkovat Sabči za empatii, pomoc a podporu. Nerad bych také opomněl rodinu a kamarády, kteří mě vždy dokázali podpořit, když to bylo potřeba.

Prohlášení

Prohlašuji, že jsem svoji bakalářskou práci vypracoval samostatně pod vedením vedoucího práce s využitím informačních zdrojů, které jsou v práci citovány.

V Brně dne 13. května 2024 .....

Filip Holoubek

Contents

Chapter 1

Introduction to supernovae

The term supernova is a compound formed from two Latin words. *Nova* is the Latin word for new, symbolizing a new star. The prefix *super-* distinguishes it from nova. Walter Baade and Fritz Zwicky coined the term in the 1930s (Osterbrock, 2001). In astrophysics, it is a term for exceedingly luminous stellar explosions. Supernovae, classified as cataclysmic variable stars, undergo a massive increase in brightness. In most cases, this process happens only once in a star's lifetime because the explosion is a very radical event that changes the characteristics of the star. After this change, the star will cease to exist or its core turns into a neutron star or a black hole.

1.1 A brief history of supernovae observations

Historically, there are not many certain records of supernovae. One of the first records dates back to 1006 when astronomers noticed a new exceptionally bright star (its remnant at fig. 1.1a). Due to the low magnitude of the star $(m_{\mathrm{v}} = -9\,\mathrm{mag})$, it was possible to observe it during the day, and even now it remains the brightest supernova witnessed in human history (Katsuda, 2017). During this period astronomers were very fortunate with bright supernovae because they had the opportunity to observe another one in less than 50 years later. In 1054, a supernova appeared in the constellation of Taurus, its remnant being visible as the Crab Nebula. More than five hundred years after these observations, in 1572, Tycho Brahe discovered a new star, a supernova, in the Cassiopeia constellation. In 1604, Brahe's student, Johannes Kepler detected the last seen supernova in the Milky Way, in the Ophiuchus constellation. These discoveries challenged the idea of the celestial sphere in the Western world at that time, which was thought to be unchanging (Carroll & Ostlie, 2017). Even though it was no longer possible to observe supernovae in the Milky Way, astronomers were lucky to find others in different galaxies. The first one was discovered by Ernst Hartwig in the Andromeda Galaxy in 1885.

Mention-worthy is the supernova discovered in 1987 in the Large Magellanic Cloud,

whose progenitor (original star) was a blue supergiant. This supernova was the closest since the development of modern instruments, making it an ideal opportunity to test new theories about the fate of massive stars.

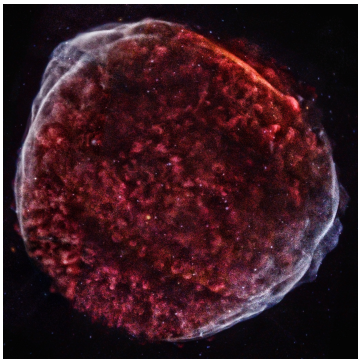

(a) SN 1006 remnant. Source: (NASA's Marshall Space Flight Center, 2017).

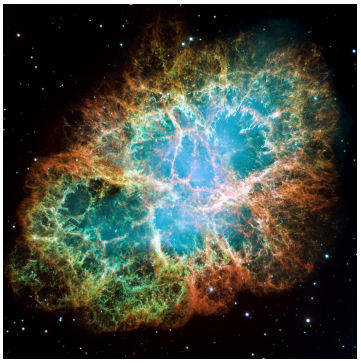

(b) SN 1054 remnant. Source: (NASA Hubble Space Telescope, 2017).

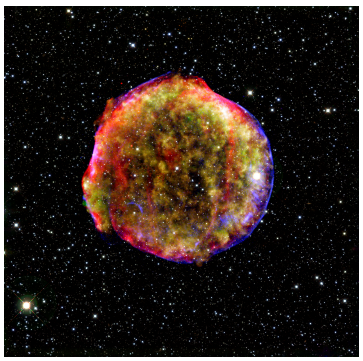

(c) SN 1572 remnant. Source: (NASA's Marshall Space Flight Center, 2019).

Figure 1.1: Remnants of historical supernovae.

1.2 Classification of supernovae

Not long after the separation of supernovae from novae, Rudolph Minkowski first attempted to classify supernovae based on spectroscopic observations of 14 events. He created two main branches - Type I and Type II. Type I was a fairly homogeneous class of 9 events. But Type II showed hydrogen signatures, which was the main difference between the classes (Gal-Yam, 2017). With more spectroscopic observations and light curves of supernovae, subclasses have been added to these classes. This led to the system still used these days. However, it does not refer to the physical basis of the supernova, but only to the observed information.

1.2.1 Type I Supernovae

This class is further subdivided according to their spectra, which indicate different physical mechanisms. These subclasses are more precise about the basis of the supernova, such as the characteristics of the progenitor, which depend on the location in the galaxy and the type of the galaxy. From the spectra, it is possible to separate Type Ia because it shows strong signatures of the Si II line at 6150 Å.

Type Ia Supernovae (SN Ia)

The most commonly observed supernova originates in a close binary system, formed by a white dwarf, the progenitor with ZAMS (Zero Age Main Sequence) mass $M < 8\,M_{\odot}$,

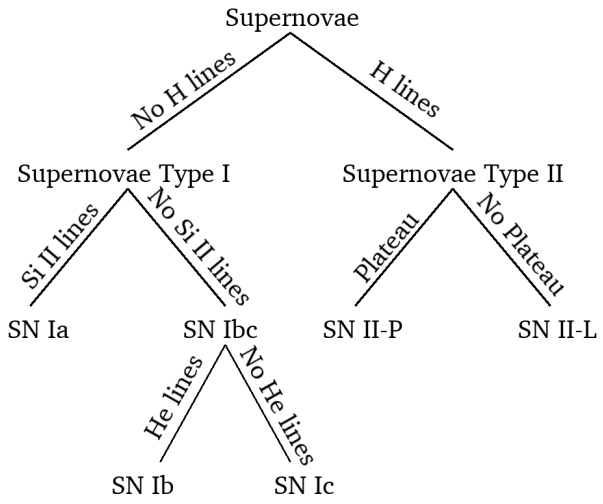

Figure 1.2: Basic classification of supernovae. From *Introduction to Modern Astrophysics* (Carroll & Ostlie, 2017).

and another star. The white dwarf is a highly dense object, which in this case draws matter from its companion. The matter accreted by the white dwarf causes it to exceed its Chandrasekhar limit $\left(M \approx 1.4\, M_{\odot}\right)$. Once this limit is reached, the temperature and pressure increase due to the gravitational compression. This leads to an uncontrollable nuclear fusion reaction of carbon and oxygen. Nucleosynthesis proceeds at a higher fuel density and lower entropy than in core-collapsed supernovae. The fusion reaction produces a large amount of energy that causes the white dwarf to collapse, accompanied by an explosion. Because of the almost identical light curves of all these supernovae, they are used as standard candles to determine distances in the universe. This is an established connection, but significant variations in the light curves have been found during the last 30 years (Kurfürst, 2010).

The mechanism of nucleosynthesis leads to the radioactive decay of ^{56}Ni into ^{56}Co and then to stable ^{56}Fe. This reaction chain produces an enormous amount of high-energy gamma rays, which are reprocessed into visible light by the supernova ejecta.

Type Ib, Ic Supernovae (SN Ib, SN Ic)

This branch of the Type I supernovae is different from the previous one. The similarities are in spectral lines, f.e. in the absence of hydrogen lines in the spectrum, and compared to the Type Ia, they lack the Si II line at 615 nm. Type Ib and Ic are distinguished by presence (SN Ib) and absence (SN Ic) of strong helium lines. The origins of type Ib and Ic are more similar to the next class (Type II SN) because they originate from the core collapse of short-lived massive stars in spiral galaxies near the sites of

recent star formation (Carroll & Ostlie, 2017).

Nowadays it appears that they are probably more closely related to Type Ia, as their origin could be found in a close binary system composed of helium stars. Another current explanation is that they may have originated from WR stars[1], as these supernovae are thought to arise from the explosion of helium or even carbon (nitrogen-oxygen) stars (Dessart et al., 2020).

1.2.2 Type II Supernovae

Type II as well as the Types Ib and Ic is the result of the core collapse of a massive star $(M > 8\,M_\odot)$. The main difference is in the spectral lines, as hydrogen lines dominate Type II spectra. In stars with masses above $10M_\odot$, carbon burning in the core continues up to the iron group. The increasing amount of iron in the core then leads to the core reaching the Chandrasekhar limit. Before this momentous event, the star looks like an onion, with an iron core and shells made of silicon, oxygen, carbon, helium, and hydrogen (in order from the core) (Branch & Wheeler, 2017; Rosswog & Brüggen, 2011).

Further energy loss processes begin when the iron core is formed at temperatures above 7.3×10^9 K. The most important one can be described as inverse β decay, where energetic electrons interact with protons, producing neutrons and antineutrinos

$$\mathrm{p} + \mathrm{e}^- \rightarrow \mathrm{n} + \nu_\mathrm{e}\,. \tag{1.1}$$

Another significant process leads to the photodisintegration of the ^{56}Fe, which absorbs the thermal high energy γ-rays

$$^{56}\mathrm{Fe} + \gamma \rightarrow 14\,^4\mathrm{He}\,. \tag{1.2}$$

As a result of these processes, there is a tremendous luminosity of neutrinos, exceeding $10^{15}\,L_\odot$, and an energy release of 300 B, which is about 10 % of the rest mass energy of $1.5\,M_\odot$ iron core. The removal of the pressure support leads to the collapse of the iron core into the proto-neutron star. Solely about 1 % of the energy must remain in the star to trigger an explosion (Branch & Wheeler, 2017; Longair, 2011).

As the Type I, it can be divided into several branches according to its light curves. The first two branches to be defined were Type IIP and Type IIL by Barbon et al. (1979).

[1] originally O-type stars with bright and wide emission lines (Vanýsek, 1980)

Type IIP and IIL Supernovae (SN IIP and SN IIL)

The Plateau type (IIP) has a typical flat evolution of light curve after the maximum with a duration of around 100 days (called plateau phase) (Branch & Wheeler, 2017). The progenitors are identified as red supergiants (RSGs), typically with masses ranging from 8 to 16 solar masses and bearing significant hydrogen envelopes. This characteristic gives rise to a plateau phase, driven by the interplay of cooling and recombination phenomena within the ejecta (Gall et al., 2015).

The Linear type (IIL) declines more steeply, which, compared to the Plateau type, indicates that the progenitors have lost the majority of their hydrogen envelope (Gall et al., 2015).

Type IIb and Type IIn Supernovae (SN IIb and SN IIn)

The main difference between these two newly classified branches and the previous ones is that the surroundings of the type IIb and IIn affect their light curve. **SN IIb**, like SN Ib, is thought to have originated in a binary system. The progenitors could be exceptionally massive stars (RSG with mass over $30\,M_{\odot}$), stripped by their companion. The progenitor loses most of its hydrogen envelope, leaving a helium-rich core, and this process produces faint hydrogen lines (Claeys et al., 2011).

SN IIn is not a supernovae type but an external phenomenon. It is caused by the interaction between the fast-moving ejecta from the supernova explosion and the dense circumstellar material (CSM) surrounding the progenitor star. The *n* in the name of this branch expresses the narrow spectral lines caused by the relatively static environment, that is ionized by the supernova before it comes into contact with its expanding envelope. (Smith, 2017).

1.2.3 Superluminous supernovae (SLSNe)

In recent years a new class of supernovae has been defined based on the discovery of extremely luminous supernovae. The first one, SN2006gy, was discovered in 2006. Typical supernovae reach luminosities of about $10^{43}\,\mathrm{erg\,s^{-1}}$, but superluminous supernovae have peak luminosities mostly about ten times higher. Based on their spectra, SLSNe can be divided into SLSNe-I and SLSNe-II. These classes are analogous to the "normal" classes of supernovae, with SLSNe-I being hydrogen-poor and SLSNe-II being hydrogen-rich (Gal-Yam, 2012).

Superluminous supernovae type I (SLSNe-I)

As mentioned in the previous paragraph, this class is associated with SN I because of the hydrogen-poor peak-light spectra. The higher peak of luminosity is not the only

feature that distinguishes them. The rise time of SLSNe-I is significantly longer, and early bumps before the first peak are more standard compared to SN Ic, with sporadic early bumps (Gal-Yam, 2019).

The energy source and mechanism of the explosion are not fully understood. The first idea, how to describe SLSNe-I was based on a newborn rapidly rotating **magnetar** as an additional energy source. It begins with the death of a massive star with high angular momentum and an extremely strong (up to even 10^{18} G) magnetic field collapsing to form a magnetar. Young magnetar, surrounded by dense ejecta in the early phase of the supernova has a rapidly rotating and magnetized core that interacts with the inner expanding layers of the SN. This leads to converting rotational inertia into high-energy radiation, from which the ejecta thermalizes X-ray photons and re-emits as the observed blackbody radiation (Gal-Yam, 2019; Prajs, 2019).

Another explanation for SLSNe-I could be **black hole accretion**, which occurs when a massive star's core collapses to form a new black hole. This accretion process releases energy that can significantly affect the optical light curve of the supernova. This process is suitable for SN-like transients, including both types of SLSNe (Dexter & Kasen, 2013; Gal-Yam, 2019).

Slowly rising SLSNe-I are caused by **radioactive decay** similar to that seen at SNe I. This theory is based on pair-instability supernovae (PISNe), which originate in very massive stars (VMS) with masses over $100M_{\odot}$ and lead to pulsations (pulsation pair-instability - PPISN - supernovae which are slightly less massive) or complete disruptions of the stars. The PISNe explosions produce large amounts of nickel, leading to very luminous supernovae. Some supernovae within this type could be classified as SLSN-R (by Gal-Yam (2012)), but this class has not been widely adopted (Gal-Yam, 2019; Sabhahit et al., 2023).

An efficient mechanism for converting the kinetic energy of the ejecta into radiation is via strong shocks from **interactions with the circumstellar medium** (CSM) around an exploding star. The origin of CSM is diverse - the result of thick solar winds, binary interactions and mergers, or stellar eruptions. CSM interactions are not so unique mechanism for powering supernovae. They appear in multiple events, including SNe IIn, SNe Ibn, unusually luminous SNe Ia, and some SN Ic events (Gal-Yam, 2019).

Superluminous supernovae type II (SLSNe-II)

The class with hydrogen-rich peak-light spectra are often accompanied by helium spectral lines. From the emission spectral line, it is possible to find similarities with SNe IIn. This leads to deriving the SLSNe-IIn branch, which has a similar origin but a higher luminosity peak. The progenitor is supposed to be mostly the Luminous Blue Variable (LBV) because of the requirement for massive ejecta and massive CSM (Gal-Yam,

2019).

Host Galaxies of the Superluminous Supernovae

The environments in which they arise can provide more information about the origin and conditions leading to the formation of SLSNe. Hydrogen-poor SLSNe tend to be found in extremely blue, low-mass dwarf galaxies, with specific star formation rates (sSFRs) that are on average 0.5 dex higher than those of main-sequence star-forming (SF) galaxies. The hosts of SLSNe-II are distinct from those of SLSNe-I, with SLSNe-II hosts being 0.8 dex more massive on average. It is assumed that there is no significant dependence of SLSNe-II on the overall properties of the host galaxy. The luminosity of SLSNe-II is determined by the intensity of the interaction rather than by the type of stellar explosion (Schulze et al., 2018).

1.3 Supernovae remnants

Supernovae are not uniform in their remnants. The progenitor of core-collapsed supernovae evolves into a compact remnant, such as a neutron star or black hole, whereas the progenitors of SN Ia do not leave anything like a compact remnant. On the other hand, the remnant of matter ejected by the supernova sweeps up the CSM and then the interstellar medium (ISM). The ejecta slows down when the mass of the material being swept up is comparable to the mass of the ejecta, and a shell-like SNR (supernova remnant) is formed. SNR is a nebular object whose brightness decreases over time (Branch & Wheeler, 2017).

An ideal example is the SNR of SN 1054, which is still expanding, and a rapidly rotating pulsating star has also been detected at its center, slowing down the decline in brightness (Vanýsek, 1980).

1.4 Significance of supernovae

As a unique and massive event, the supernova plays an important role in the universe. Supernova explosions produce heavier elements, enriching the surrounding space ejected during the explosion. This applies not only to the new generation of stars but also to planetary systems and planets.

The energy released can stimulate the formation of new stars, but it can act as an inhibitor as well. They may also be a significant aspect in galaxy evolution, where they can eject matter from galaxies in supernova-heated galactic winds.

Supernovae are extremely bright objects that can be seen from great distances, making them ideal for measuring extragalactic distances. They are used to determine

the value of the Hubble constant (H_0) and to trace the history of cosmic expansion.

It has also been suggested that neutrinos from explosions may have affected the molecular structure of amino acids in the solar system and directly impacted life on Earth (Alsabti & Murdin, 2017; Branch & Wheeler, 2017).

Chapter 2

Light curves and spectroscopic properties

As mentioned in the previous chapter, the classification of supernovae is historically determined by light curves and spectroscopy. More details about these properties can be found in the following chapter.

2.1 Light curves

A light curve is a graph of the brightness as a function of time (Carroll & Ostlie, 2017) and is widely used for variable stars. Although supernovae are not periodic-like variable stars, the light curve is one of the most valuable information about these events.

2.1.1 SNe Ia

At the beginning, the light curve of a typical SN Ia is powered by a thermodynamical expansion, which is then followed up by the radioactive decay chain described in section 1.2.1. The luminosity ($L_{\mathrm{UVOIR}} \gtrsim 10^{43}\ \mathrm{erg\,s^{-1}}$) peaks about 20 days after the explosion. Its maximum absolute visible magnitude can reach $M_{\mathrm{V}} = -19.3$ mag. The velocity ($v \simeq 10,000\ \mathrm{km\,s^{-1}}$) in the photosphere, obtained from the blue shifts and widths of the spectral lines, allows the temperature in the photosphere to be an order of $T_{\mathrm{ph}} \sim 10^4$ K.

After the maximum light, the UVOIR (UV, optical, and infrared) luminosity transcends the luminosity of the radioactivity for a short time as the accumulated energy escapes. As the ejecta expands, the increasing fraction of gamma rays can escape as the column density and gamma-ray optical depth decreases with time as t^{-2}, and the luminosity of the radiation again dominates over the UVOIR luminosity.

After about 200 days, virtually all the gamma rays escape, and for the next few hundred days, the light curve depends on the positrons. Positrons slow down and

annihilate with electrons to produce gamma rays. Until this energy deposition is dominant, the bolometric light curve should correspond to the ^{56}Co decay rate. However, in the case of the weak or "radially combed" magnetic field, more positrons escape before the deposition of all their kinetic energy and the light curve decreases faster (Branch & Wheeler, 2017).

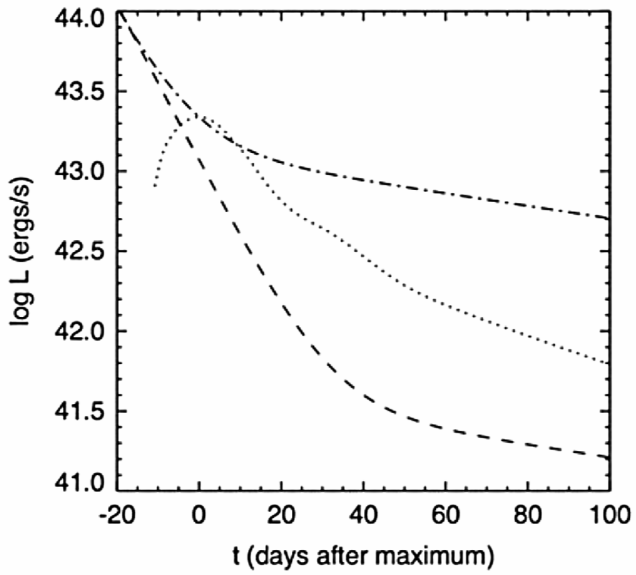

Figure 2.1: The dotted curve represents a UVOIR light curve of a typical SN Ia. The dashed line shows the radioactive luminosity with complete trapping of decay products. The dash-dotted line corresponds to complete gamma-ray escape and complete positron trapping. From *Optical light curves of Supernovae* (Leibundgut & Suntzeff, 2003).

2.1.2 SNe Ib and SNe Ic

Compared to SNe Ia, these types are more occasional, and therefore their light curves are not as well studied. Their peak brightness is about one magnitude lower than that of SN Ia, in the *R*-band $M_{\mathrm{R,\,SNIb}} = (17.9 \pm 0.9)$ mag and $M_{\mathrm{R,\,SNIc}} = (18.3 \pm 0.6)$ mag. From the photospheric velocities, it is at least possible to determine the approximate values of the outburst properties, such as the ejecta mass, $M_{\mathrm{ej,\,SN\,Ib,\,Ic}} \approx 2\,M_{\odot}$, and the kinetic energy $E_{\mathrm{k,\,SN\,Ib,\,Ic}} \approx 10^{51}$ erg. The typical ^{56}Ni mass could be obtained from the light curves, $M_{\mathrm{Ni,\,SN\,Ib,\,Ic}} \approx 0.2\,M_{\odot}$ (Drout et al., 2011).

The progenitor eruption produces an X-ray flash when the shock wave from the core reaches the photosphere. It is considered that a fading UVOIR fireball[2], visible for several days, may follow the outburst flash. After the fireball phase, and in the

[2]Longer dimmer phase of subsequent cooling (Branch & Wheeler, 2017)

absence of circumstellar interactions, the light curve is powered by Ni and Co decay, suggesting that the basic physical processes are similar to those in SN Ia (Branch & Wheeler, 2017).

2.1.3 SNe IIL and SN IIP

The SNe II are rising rapidly and the mean peak absolute magnitude in the *R*-band is $M_{\mathrm{R}} = -17.14$ mag (Gal-Yam, 2017). The shock generated by the core collapse is expected in the photosphere within hours to days, the breakout producing a bright and brief pulse of UV radiation and X-rays. The shock wave is also accompanied by heating and ionization of the material in the envelope. The gradual ionization of the lower layers facilitates the emission of the first optical radiation from the ejecta.

When the fireball phase, lasting up to several weeks, cools below 10,000 K, hydrogen in the most distant layers begins to recombine. As the cooling and recombination from the outside to the inside continue, the temperature gradually stabilizes at about 5,500 K. Additionally, the luminosity is going to be almost constant. This leads to the light curve plateau, which occurs for about 100 days with a total radiated energy of about 10^{49}erg. The descent in the final phase of the plateau is caused by the recombination front (location inside the envelope with the same temperature as the temperature of hydrogen recombination) reaching the hydrogen envelope base. The plateau phase distinguishes SNe IIL from SNe IIP because SNe IIL have an almost linear decrease instead of a plateau. This different evolution of the light curve causes a magnitude difference of approximately two magnitudes at the end of these phases (Arcavi, 2017; Branch & Wheeler, 2017; Kirshner, 1990). The difference between linear and plateau type II supernovae is shown in Figure 2.2.

2.1.4 SNe IIb and SNe IIn

It is possible to find similarities between the light curves of SNe IIb compared to SN Ib. They have a comparable shape, as the luminosity minimum is associated with the fireball phase and rises to the secondary maximum and tail phase, both of which are powered by the decay of ^{56}Co (Branch & Wheeler, 2017). Their mean peak magnitude is about $M_R = -17.9$ mag (Gal-Yam, 2017).

The brightest of the SN II type are SNe IIn with an average peak around $M_R = -18.8$ mag, which is caused by interaction with CSM. SNe IIn also have immense inconsistency in luminosity and the shape of the light curves. This inconsistency could provide more information about the CSM, possibly caused by the diversity of asymmetries in the density structure and mass of the CSM (Arcavi, 2017; Gal-Yam, 2017).

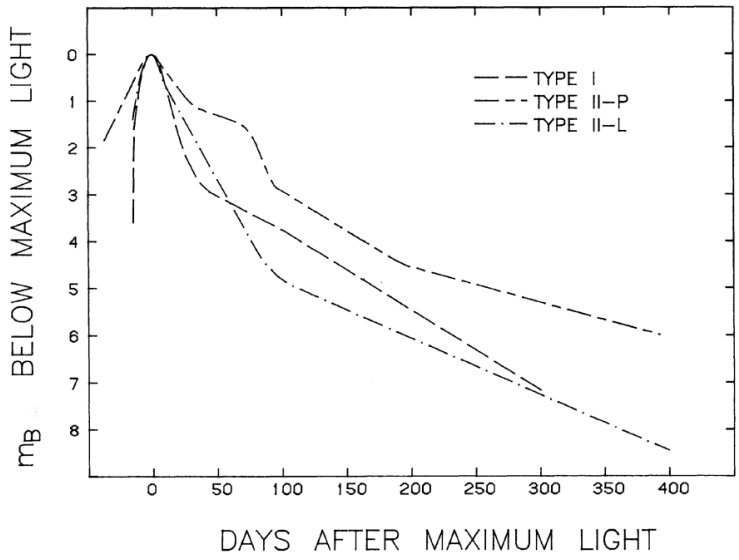

Figure 2.2: Comparison of the SN IIP, SN IIL, and SN I mean blue light curves. From *A comparative study of supernova light curves* (Doggett & Branch, 1985).

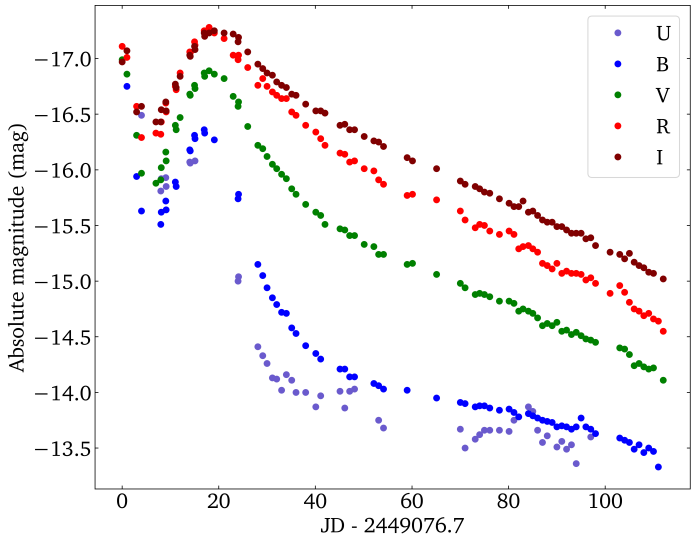

Figure 2.3: Light curve of Type IIb SN 1993J. Data from *UBVRI Photometry of SN 1993J in M81: The First 120 Days* (Richmond et al., 1994).

2.1.5 SLSNe-I and SLSNe-II

SLSNe-I light curves are typical for a slow evolution before and after the peak, frequently accompanied by short-term undulations and bumps. Quintessential peak magnitudes are detected in the g-band between $M_g = -22.5$ mag and $M_g = -21.14$ mag and a typical mean peak is around $M_{\text{unfiltered}} = -21.7$ mag.

As mentioned above, SLSNe-I characterize a slower rise time ranging from 20 days

to more than 100 days, for which the difference between the first detection and the peak defines the lower limit. As well as the rise, the decay is slow, to the extent < 0.01 to 0.08 mag d^{-1} in the restframe g-band.

In some cases, early and late bumps could be found. For the early bumps, the typical duration ranges from ten days to several weeks, with magnitude peaks ranging from -19 mag to -21 mag, both higher limits of the ranges being extreme cases. Late bumps typically appear up to 100 days after the peak, with a duration of about 20 days and a deviation of roughly 20 % from the fit of the bolometric light curve.

SlSNe-II have comparable light curve properties to SLSNe-I, only the mean peak is slightly lower $M_R = -21.1$ mag (Gal-Yam, 2019). The light curves of both branches are compared with typical light curves of other classes of supernovae in Figure 2.4.

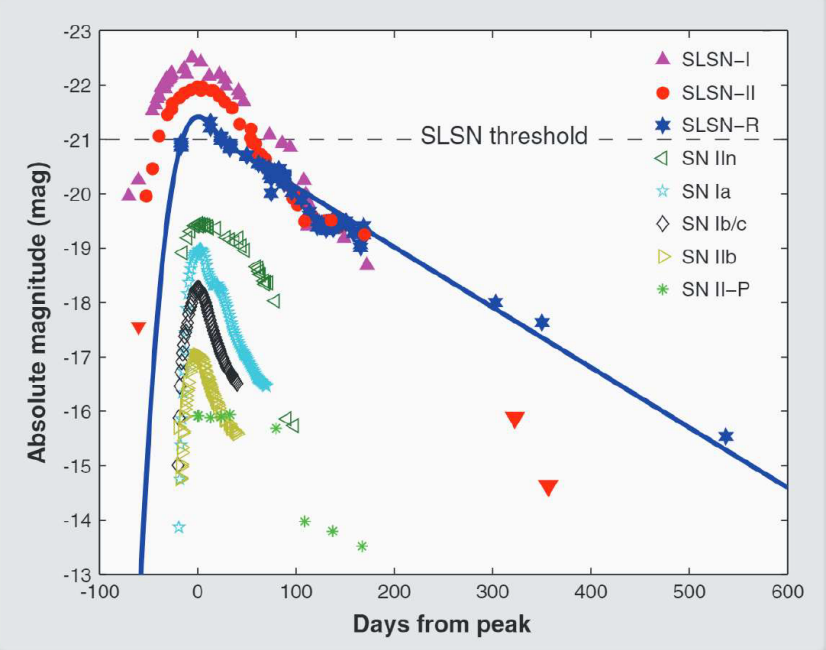

Figure 2.4: Light curves of SLSNe compared to other SNe classes. From *Luminous Supernovae* (Gal-Yam, 2012).

2.2 Spectroscopic properties

Spectroscopy is a powerful tool that analyses the light emitted, absorbed or scattered by celestial objects. Spectra have been used to classify stars, determine redshifts and properties of galaxies, or the chemical structure of stellar atmospheres and the interstellar medium (Birney et al., 2006).

2.2.1 SNe Ia

The spectral lines of SNe Ia (at figure 2.5) show no sign of hydrogen or helium lines. It is distinguished from other hydrogen-poor supernovae by exceedingly deep Si II absorption lines around 6100 Å. Combined with the dominance over O absorption lines, this produces a characteristic large Si/O depth ratio. Other distinctive lines near maximum light are Ca II, S II, and Mg II. Within two weeks after maximum light they are supplemented by a mixture of Fe II lines, complemented by Co II lines. These new lines dominate the spectrum for at least 100 days, confirming the iron-rich core (Branch, 1990; Gal-Yam, 2017; Filippenko, 1997).

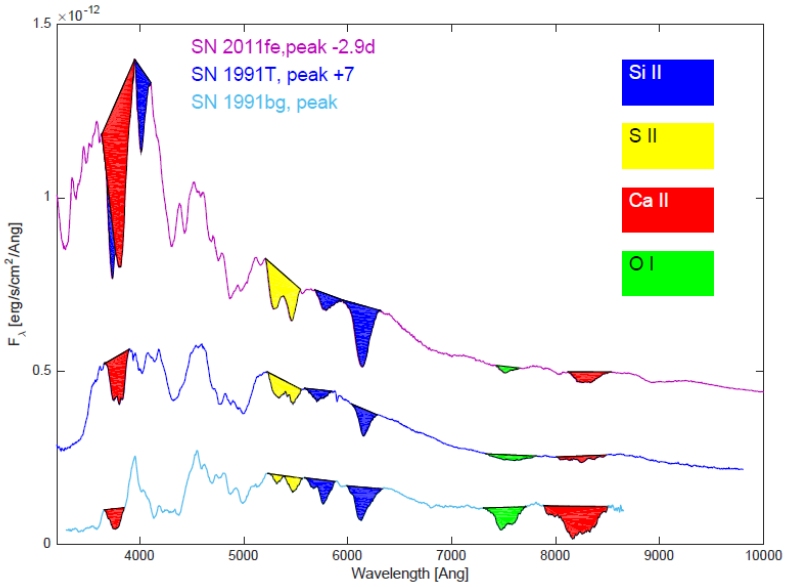

Figure 2.5: Spectra of SN Ia representatives, with SN 2011fe being considered the classic case. From *Observational and Physical Classification of Supernovae* (Gal-Yam, 2017).

2.2.2 SNe Ib and SNe Ic

The optical spectrum of helium-rich **SNe Ib** is characterized by strong lines of He I, accompanied by C II, O I, Ca II and Fe II lines. A small amount of hydrogen is often shown at low optical depth in the early phase but it can still be distinguished from hydrogen-rich SN IIb (Branch, 1990) (Branch & Wheeler, 2017) (Filippenko, 1997).

The spectral lines of **SNe Ic** lack signs of H and He I lines, but have a stronger O I absorption line near the peak than SNe Ib. Another typical attribute is shallower absorption lines around 6150Å, mainly due to the dominance of Si II absorption rather than hydrogen. This distinction is crucial in distinguishing SN Ic from other types of supernovae, such as Type Ib, which have stronger helium features (Branch, 1990; Branch & Wheeler, 2017).

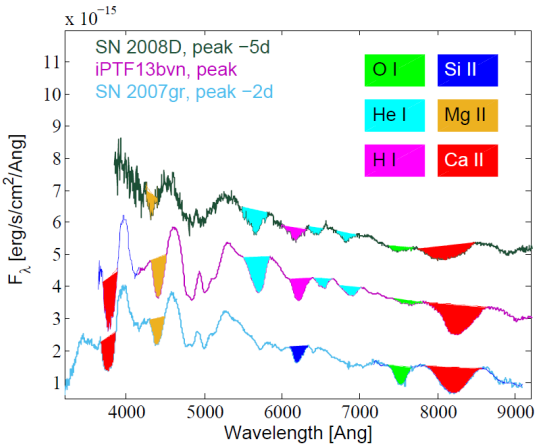

(a) Spectra of regular SN Ib representatives. From *Observational and Physical Classification of Supernovae* (Gal-Yam, 2017).

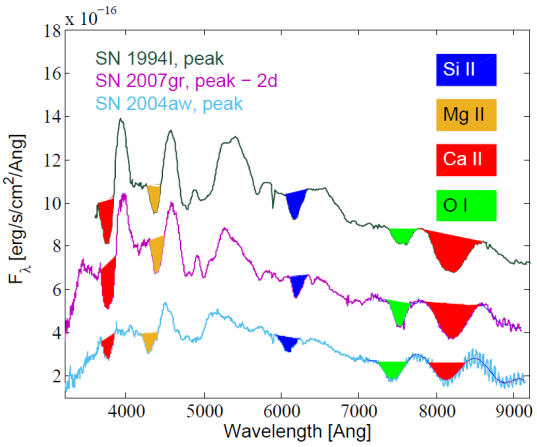

(b) Spectra of regular SN Ic representatives. From *Observational and Physical Classification of Supernovae* (Gal-Yam, 2017).

Figure 2.6: The spectrum of regular SN Ib and SN Ic representatives.

2.2.3 SN IIL and SN IIP

Type II SNe typically exhibits strong, broad hydrogen lines, particularly Balmer Hα, in their spectra, especially in the early stages of their evolution. These hydrogen lines are a prominent feature that distinguishes SNe II from other types of supernovae. In addition to hydrogen, SN II spectra also show lines from other elements such as He I, C, O, iron group elements - Fe II and other metal lines. **SN IIP** events have a plateau phase with strong and broad hydrogen lines, which persist for a longer period, while **SN IIL** events have rapidly declining light curves with weaker and narrower hydrogen lines fading more rapidly (Branch, 1990; Branch & Wheeler, 2017; Gal-Yam, 2017). The difference between SN IIL and SN IIP can be seen in Figure 2.7.

2.2.4 SN IIb and SN IIn

The spectral lines of **SN IIb** (at Figure 2.8a) are very similar to those of SN Ib, as some of SN Ib also show some hydrogen signatures. In the *Observational and Physical Classification of Supernovae* in the *Handbook of Supernovae* by Gal-Yam (2017), the reclassification is considered, as Ib should be reserved for events without hydrogen signatures.

SNe IIn (at Figure 2.8b) are characterized by strong and relatively narrow Balmer emission lines, including complex profiles of Hα, Hβ and Hγ, alongside helium lines, for example He I. In addition, their spectra show metal lines of elements such as Fe, Ca, Si and S, reflecting the composition of the ejecta and CSM. These spectral features arise from the interaction between the supernova ejecta and a slowly moving CSM, resulting in diverse profiles that reveal the complex dynamics of the explosion and

its surroundings.

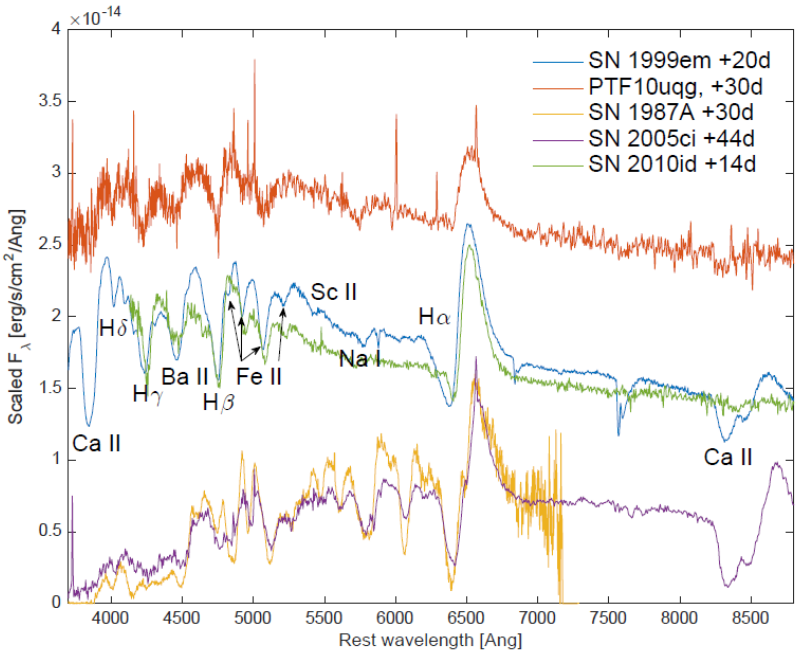

Figure 2.7: Spectra of Type II SNe. SN 1999em is SN IIP, PTF 10uqg is SN IIL and the remaining three represent slowly rising events. From *Observational and Physical Classification of Supernovae* (Gal-Yam, 2017).

2.2.5 SLSNe-I and SLSNe-II

The typical spectrum of hydrogen-poor **SLSNe-I** (at Figure 2.9a) shows strong absorption lines from dense O II transitions in the blue wavelengths (3000 Å to 5000 Å) in the visible light spectra. Several prominent absorption features are observed in the UV, while the red part of the spectrum typically shows weaker features of O I and C II. During the hot photospheric phase, SLSNe-I spectra show absorption from numerous O II transitions, evolving to resemble those of more normal SNe Ic around the peak in later phases (weeks to months after the peak) (Gal-Yam, 2017).

SLSNe-II (at Figure 2.9b) are not so well studied, nor are their spectra. However, because of their comparable origin, it is possible to look for similarities between SLSNe-II and SN IIn. The spectroscopic evolution of **SLSNe-II** begins with simple blue spectra, evolves to more complex profiles and culminates, after several hundred days, in spectra dominated by residual Hα emission with minimal continuum (Gal-Yam, 2017).

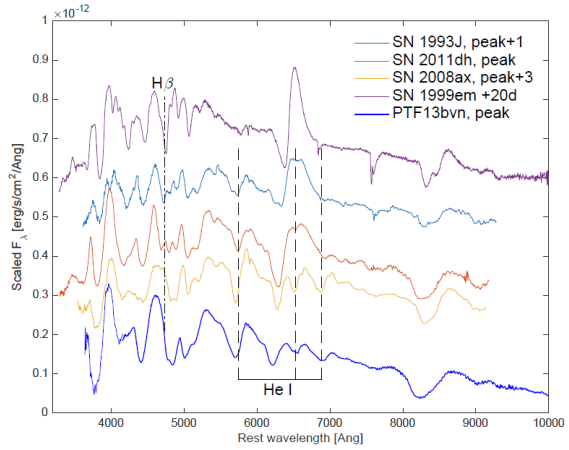

(a) The spectra of SNe IIb (SN 1993J, SN 2011dh, SN 2008ax) in comparison with regular SN II (SN 1999em) and SN Ib (PTF13bvn). From *Observational and Physical Classification of Supernovae* (Gal-Yam, 2017).

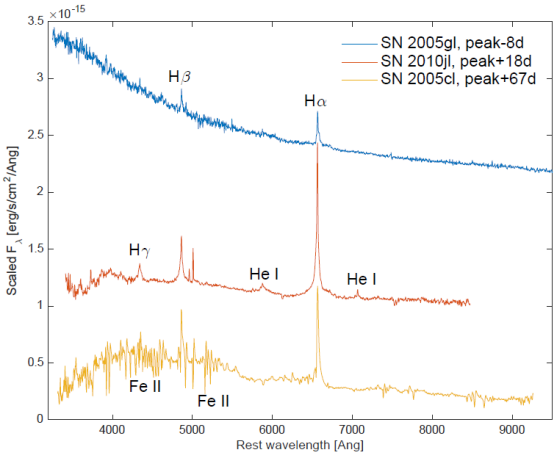

(b) Optical spectra of SN IIn representatives at pre-peak phase (SN 2005gl), post-peak phase (2010jl) and late phase (SN 2005cl). From *Observational and Physical Classification of Supernovae* (Gal-Yam, 2017).

Figure 2.8: The spectrum of regular SN IIb and SN IIn representatives.

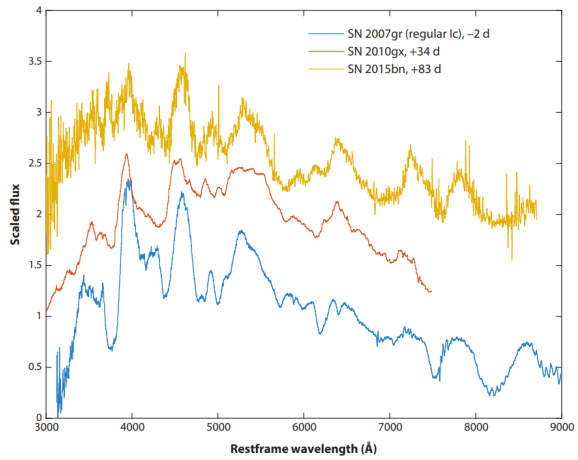

(a) Spectra of SLSNe-I representatives at pos-peak cool-photospheric (SN 2010gx and SN 2015bn *The Most Luminous Supernovae*) in comparison with normal SN Ic at peak (SN 2007gr) (Gal-Yam, 2019).

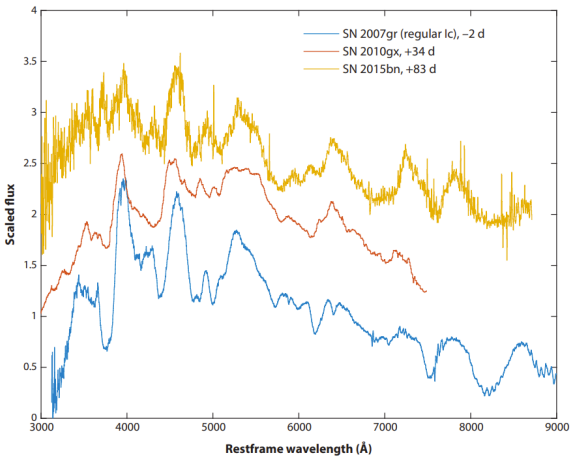

(b) Spectra of SLSN-II before and after the peak (SN 2008es) and SLSNe-IIn, 34 and 83 days after the peak (SN 2008am and PTF10qaf). From *The Most Luminous Supernovae* (Gal-Yam, 2019).

Figure 2.9: Spectra of regular SSLNe-I and SLSN-II representatives.

Chapter 3

Interactions with CSM

Since this work focuses on superluminous supernovae, especially those in whose morphology of the CSM plays a significant role, it would be suitable to get a deeper insight into these interactions. The interactions of supernovae with CSMs are very well described in *Interacting Supernovae: Types IIn and IIb* by Nathan Smith (2017) in the *the Handbook of Supernovae*, and the following paragraphs summarise that work.

After the SN explosion within the dense CSM, the forward shock is directed outward into the CSM, while the backward shock in the CSM is directed back into the SN ejecta. These interactions create an environment that can be divided into four zones (shown at Figure 3.1):

1. Zone with photoionized and unshocked (pre-shock) CSM outside the forward shock.
2. Zone containing shocked CSM, which was hit by a forward shock.
3. Zone encompassing the decelerated (shocked) SN ejecta that have encountered the reverse shock.
4. Zone describing a freely expanding SN ejecta.

In the regular type supernovae, only the emission from zone 4 has been observed at visible wavelengths. Zones 2 and 3 are occasionally detectable in X-rays, provided that the CSM is sufficiently dense. The zone 1 is detected only in exceptional cases in the absorption lines. In contrast, for interacting SNe, each of these four zones can be involved in the emission spectrum at visible wavelengths. The zones 2 and 3 encompass the so-called contact discontinuity which is the region of contact between the two gas volumes - the expanding SN envelope and the initially pre-explosion CSM. This discontinuity zone is then usually perturbed by instabilities caused mainly by intense radiative cooling.

Early shock radiation produces an ionized early spectrum, often lasting from a day to several weeks or months. During this phase, the unshocked CSM hosts the electron-

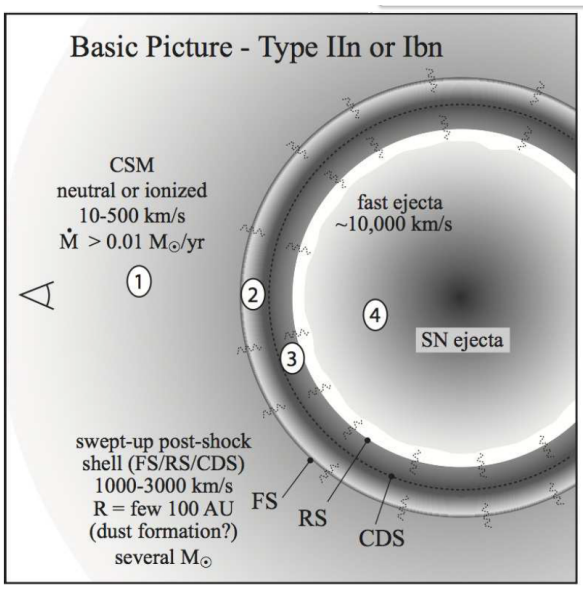

Figure 3.1: SN interacting with CSM. From *Interacting Supernovae: Types IIn and IIb* (Smith, 2017).

scattering continuum photosphere, which masks the shock. The resulting spectrum typically shows a smooth blue continuum with narrow emission lines.

As the density of the pre-shock CSM decreases with increasing radius, the photosphere shrinks into zones 2 and 3. In this phase, it is possible to see transformations in the spectrum, usually around the time of the luminosity peak. Zones 2 and 3 may collapse and merge due to the strong radiative cooling. The cooled gas is very dense and forms the so-called cold dense shell that emits strongly in lines such as Hα or He I when being reheated by the shock.

After the peak, the continuum photosphere might recess into zone 4 within the expanding ejecta. In case of weak or short-lived CSM interactions, observing the typical spectrum of the SN becomes possible. Although the SN itself may fade in a few months, interactions with the CSM can extend the high luminosity from months to years. The duration of the bright CSM interaction is thus primarily defined by the pre-SN mass loss, that is, by the total amount of mass ejected from SN progenitor before the explosion, not by the explosion itself.

The total radiated energy during SN II interacting with CSM can reach more than 50 % of the total kinetic explosion energy (which is typically 10^{51} erg for a "standard" SN), whereas normal SN II only reaches about 1 %. The total luminosity of the CSM interactions, which depends on the rate at which the CSM enters the forward shock depending on the pre-explosion mass loss rate of the progenitor $\dot{M}$, is equal to

$$L = \frac{1}{2} w V_{\mathrm{CDS}}^3 \,. \tag{3.1}$$

Here the w is the wind density parameter, which can be determined as $w = 4\pi R^2 \rho$

or $w = \frac{\dot{M}}{V_{\mathrm{CSM}}}$. V_{CDS} express the value of the evolving speed of the CDS measured from intermediate-width lines in optical spectra (Smith, 2017).

The observed subtypes of SNe with CSM interactions are Type IIn, Type IIn-P, Type IIn/Ia or Ia-CSM, Type Ibn, and the hypothetical Type Icn.

Chapter 4

Used programs and codes

4.1 SNEC

The *S*uper*N*ova *E*xplosion *C*ode is a versatile open-source code made by Morozova et al. (2015a) for simulating supernova explosions and generating corresponding light curves. SNEC utilizes a spherically symmetric (1D) model and uses Lagrangian hydrodynamics together with the equilibrium diffusion radiation transport to simulate the dynamics of supernova events. Lagrangian hydrodynamics is in the mass coordinate system, unlike Eulerian hydrodynamics, which is in the spatial coordinates. One of the key strengths of the SNEC is its ability to systematically and rapidly explore variations in stellar properties to understand how these changes affect the resulting light curves. This feature is crucial for studying the different photometric behaviors of various types of supernovae, such as SNe IIP (with nearly constant plateau luminosity), SNe IIL (with linearly decreasing magnitude), and SNe IIb (with hydrogen signatures but similar to SNe Ib).

4.1.1 Hydrodynamic equation

The three fundamental equations are derived from Lagrangian hydrodynamics in addition to the radiation diffusion term, written to the first order in $\frac{v}{c}$. A mass conservation equation (continuity equation)

$$\frac{\partial r}{\partial m} = \frac{1}{4\pi r^2 \rho}, \tag{4.1}$$

a momentum equation

$$\frac{\partial v}{\partial t} = -\frac{Gm}{r^2} - 4\pi r^2 \frac{\partial P}{\partial m} - 4\pi \frac{\partial \left(r^2 Q\right)}{\partial m}, \tag{4.2}$$

and an energy equation

$$\frac{\partial e}{\partial t} = \frac{P}{\rho}\frac{\partial \ln \rho}{\partial t} - 4\pi r^2 Q \frac{\partial v}{\partial m} - \frac{\partial L}{\partial m} + \epsilon_{\mathrm{Ni}}\,. \tag{4.3}$$

The mass coordinate can be expressed as $m = \int_0^r 4\pi r'^2 \rho(r')\,\mathrm{d}r'$, r is the radius, ρ is the density, ϵ is the specific internal energy, P is the pressure, $v = \frac{\partial r}{\partial t}$ is the velocity of the matter, Q is the artificial viscosity (the viscosity term added to damp the numerical oscillations in velocity), and G is the gravitational constant. The ϵ_{Ni} in the equation 4.2 is the specific energy deposition rate due to the radioactive decay of ^{56}Ni which is equal to the time-dependent rate of energy release per gram of radioactive nickel ϵ_{rad}, multiplied by the deposition function d. The energy release per gram of radioactive nickel ϵ_{rad} is described as

$$\epsilon_{\mathrm{rad}} = 3.9\times10^{10}\exp\left(-\frac{t}{\tau_{\mathrm{Ni}}}\right) + 6.78\times10^{9}\left[\exp\left(-\frac{t}{\tau_{\mathrm{Co}}}\right) - \exp\left(-\frac{t}{\tau_{\mathrm{Ni}}}\right)\right]\mathrm{erg\,g^{-1}\,s^{-1}}\,, \tag{4.4}$$

where $\tau_{\mathrm{Ni}} = 8.8$ d and $\tau_{\mathrm{Co}} = 113.6$ d are the mean lifetimes of ^{56}Ni and ^{56}Co. The deposition function d is described as

$$d = \frac{1}{4\pi}\oint\left(\frac{4\pi\kappa_\gamma}{\epsilon_{\mathrm{rad}}}\right) I\,\mathrm{d}\omega\,, \tag{4.5}$$

where ω is the solid angle, I is the energy-integrated intensity and κ_γ is effective gamma-ray opacity, which is assumed to be purely absorptive, energy independent and equal to $\kappa_\gamma = 0.06\,Y_{\mathrm{e}}$ cm^2 g^{-1}, where Y_{e} is electron fraction (Morozova et al., 2015a).

4.1.2 Input parameters and equation of state

The input parameters for the model of pre-SN profiles could be obtained from another open-source code, MESA (*M*odules for *E*xperiments in *S*tellar *A*strophysics), produced by Paxton et al. (2011). MESA provides a suite of robust, efficient, and thread-safe libraries for simulating various aspects of stellar evolution, including structure, composition, and physical processes within stars.

It is also possible to vary the parameters for the explosion itself. One of the most important is the equation of state (EOS) of which SNEC provides two. The first is an ideal single-particle Boltzmann gas EOS. Its main purpose is to demonstrate the ability to pass the Sedov blast wave test. The shock wave is a strong spherical explosion in the atmosphere that tests a homologous expansion ($v \sim r$, i.e. the velocity is proportional to the distance from the explosion focus) under the conditions described in the article Sedov (1946). Primarily there is the Paczyński EOS, which is a simplified analyt-

ical EOS for a mixture of ions, photons, and semidegenerate/semirelativistic electrons (Morozova et al., 2015a,b).

As SNEC can only produce a 1D model, data from SNEC was used as input to a more advanced multidimensional code - CASTRO.

4.2 Modeling the equatorial disk and bipolar lobes

For modeling the CSM (equatorial disk and bipolar lobes similar to Homunculus nebula) with which the SN interacts, was used a part of the code made by Kurfürst et al. (2020) for hydrodynamic simulations of SN interaction with CSM.

For the initial state, were used the following analytical approximations: The surrounding spherically symmetric stellar wind density ρ_{wind} is set to

$$\rho_{\text{wind}} = \frac{\dot{M}_{\text{wind}}}{4\pi r^2 v_{\text{wind}}} = \rho_{0,\,\text{wind}} \left(\frac{R_\star}{r}\right)^2, \tag{4.6}$$

where $\dot{M}_{\text{wind}} = 10^{-6}\, M_\odot\, \text{yr}^{-1}$ is the stellar spherical wind mass loss rate corresponding to an RSG typical mass loss rate, v_{wind} is the typical wind velocity which is about $15\,\text{km}\,\text{s}^{-1}$, r is the spherical distance. Additionally, $\rho_{0,\,\text{wind}}$ is the wind density at (or near) the stellar surface, and $R_\star$ is the stellar radius.

Equatorial disk

The total density distribution was set in the case of the SN-disk interaction model as a sum of a spherically-symmetric wind and an equatorially-concentrated disk. The disk density ρ_{disk} was set following Kurfürst & Krtička (2019) as

$$\rho_{\text{disk}} = \rho_{0,\,\text{disk}} \left(\frac{R_\star}{r}\right)^w \exp\left[\frac{2\left(\sin\theta - 1\right)}{(H/\mathscr{R})^2}\right], \tag{4.7}$$

where $\rho_{0,\,\text{disk}} \approx 4 \times 10^{-9}\,\text{g}\,\text{cm}^{-3}$ is the mass density (arbitariry overscaled, due to the overflow from Roche lobes) at the base of the disk midplane (close to the surface of the SN progenitor star), $w = 2$ is the density profile power-law index, θ is the polar angle (in equatorial disk midplane, $\theta = \frac{\pi}{2}$). H is the disk vertical scaleheight, defined as (Kurfürst et al., 2020; Kurfürst & Krtička, 2019) $H = c_S/\Omega$, where $\Omega = \sqrt{GM_\star/\mathscr{R}^3}$ is the disk Keplerian angular velocity, $\mathscr{R}$ is the cylindrical distance from the star-disk system's rotational axis, and c_S is determined as slowly decreasing power law profile with the approximate radial power -0.4 and is dependent on the stellar progenitor effective temperature being approximately 4000 K.

Bipolar lobes

To create the CSM as a bipolar nebula similar to the Homunculus, parameters for five major components of the nebula were assumed. These components are pre-outburst wind, major eruption, first post-outburst wind, minor eruption, and final post-outburst wind using equations.

However, the size of the homunculus had to be reduced because the interactions did not occur within a year. Also, the duration of the two mass ejections had to be reduced, resulting in a lower total nebula mass, $1.7 \times 10^{-2}\, M_{\odot}$.

The initial temperature structure of the underlying stellar wind was set similarly to the disk. The temperature of two expanding rings was determined to be $T = 20\,\mathrm{K}$ by the polytropic approximation and the ideal gas law (Kurfürst et al., 2020).

4.3 CASTRO

CASTRO is a code that solves the multi-component compressible hydrodynamic equations with a general equation of state (EOS) for astrophysical flows. Additional physics includes self-gravity, nuclear reactions, and radiation. CASTRO operates within an Eulerian grid and includes adaptive mesh refinement (AMR). The AMR approach uses a nested hierarchy of logically rectangular grids with simultaneous refinement of the grids in both space and time (Almgren et al., 2010).

4.3.1 Hydrodynamic equations

In CASTRO, equations of fully compressible hydrodynamics are developed as forward in time. The equation of conversation of mass (continuity)

$$\frac{\partial \rho}{\partial t} = -\nabla \cdot (\rho \mathbf{u}) + S_{\mathrm{ext},\,\rho}\,, \tag{4.8}$$

and a momentum equation

$$\frac{\partial (\rho \mathbf{u})}{\partial t} = -\nabla \cdot (\rho \mathbf{u}\mathbf{u}) - \nabla p + \rho \mathbf{g} - S_{\mathrm{ext},\,\rho\,\mathbf{u}}\,, \tag{4.9}$$

an energy equation

$$\frac{\partial (\rho E)}{\partial t} = -\nabla \cdot (\rho \mathbf{u} E + p\mathbf{u}) + \rho H_{\mathrm{nuc}} + \rho \mathbf{u} \cdot \mathbf{g} + S_{\mathrm{ext},\,\rho E}\,. \tag{4.10}$$

Here ρ is the mass density, $\mathbf{u}$ is the velocity vector and E is the total energy per unit mass. The total energy is equal to $E = e + \frac{\mathbf{u}\cdot\mathbf{u}}{2}$, where e is the specific internal energy. The gravitational acceleration vector is marked as $\mathbf{g}$. From the user-supplied EOS, there

is defined the pressure p. External source terms for the mass conservation equation $S_{\text{ext},\rho}$, energy equation $S_{\text{ext},\rho E}$ and momentum equation $S_{\text{ext},\rho\,\mathbf{u}}$ are also user-specified. For reacting flaws the equation is developed for mass fractions X_k (with limitation $\sum_k X_k = 1$):

$$\frac{\partial\left(\rho X_k\right)}{\partial t} = -\nabla\left(\rho\mathbf{u}X_k\right) + \rho\dot{\omega}_k + S_{\text{ext},\rho X_k}\,, \tag{4.11}$$

where the production rate $\dot{\omega}_k$ for species k is defined by a user-supplied reaction network, similar to H_{nuc}. Passive advection quantities C_k^{adv} and auxiliary variables C_k^{aux} are also included in CASTRO. The variables $\mathbf{U} = \left(\rho,\, \rho\mathbf{u},\, \rho E,\, \rho X_k,\, \rho C_k^{\text{adv}},\, \rho C_k^{\text{aux}}\right)$ are referred as conserved (Almgren et al., 2010).

4.3.2 Equation of state

Castro has a wide range of options for user-supplied EOSs, but each EOS must provide an interface for acquiring thermodynamic quantities from ρ, e, and X_k. The EOS used for the simulations in this thesis was one of the EOSs supplied with the CASTRO distribution, the gamma-law EOS, which describes the relationship between temperature and pressure in terms of density and e

$$p = \rho e(\gamma - 1) = \frac{\rho T k_B}{\mu m_p}\,. \tag{4.12}$$

Here γ is the ratio of heats (e.g., $\gamma = \frac{5}{3}$ for a monoatomic gas), m_p is the mass of the proton, k_B is the Boltzmann's constant and the mean molecular weight μ is equal to

$$\frac{1}{\mu} = \sum_k \frac{X_k}{A_k}\,, \tag{4.13}$$

where A_k is the atomic weight of species k. But that was just an example because CASTRO includes more EOSs such as Helmholtz (including degenerate/relativistic electrons, ions as a perfect gas and radiation) or Lattimer-Sweaty (describing dense nuclear matter) (Almgren et al., 2010).

4.3.3 Radiation

CASTRO is also able to calculate with radiation, but this has to be considered in the hydrodynamic equations. The equations of Gray Radiation Hydrodynamics are used to describe the hydrodynamics with the radiation together. The authors used a variation of the Gray Radiation Hydrodynamics equations, keeping terms up to $O(v/c)$ and dropping all insignificant terms for streaming, static diffusion, and dynamic diffusion

limits. The flux limiter λ approximation was adopted as

$$\lambda = \frac{2+R}{6+3R+R^2}\,, \tag{4.14}$$

$$R = \frac{|\nabla E_r^{(0)}|}{\chi_{\mathrm{R}} E_{\mathrm{r}}^{(0)}}\,. \tag{4.15}$$

Here χ_{R} is the Rosseland mean of the sum of the absorption and scattering coefficients and $E_{\mathrm{r}}^{(0)}$ is equal to $E_{\mathrm{r}}^{(0)} = E_{\mathrm{r}} + 2\frac{\lambda}{\chi_{\mathrm{R}}}\frac{\mathbf{u}}{c}\cdot\nabla E_{\mathrm{r}} + O\left(\frac{v^2}{c^2}\right)$. The equations of radiation hydrodynamics are

$$\frac{\partial \rho}{\partial t} + \nabla\cdot\left(\rho\mathbf{u}\right) = 0\,, \tag{4.16}$$

$$\frac{\partial\left(\rho\mathbf{u}\right)}{\partial t} + \nabla\cdot\left(\rho\mathbf{u}\mathbf{u}\right) + \nabla p + \lambda\nabla E_{\mathrm{r}} = 0\,, \tag{4.17}$$

$$\frac{\partial\left(\rho E\right)}{\partial t} + \nabla\cdot\left(\rho E\mathbf{u} + p\mathbf{u}\right) + \lambda\mathbf{u}\cdot\nabla E_{\mathrm{r}} = -c\kappa_{\mathrm{P}}\left(aT^4 - E_{\mathrm{r}}^{(0)}\right)\,, \tag{4.18}$$

$$\frac{\partial E_{\mathrm{r}}}{\partial t} + \nabla\cdot\left(\frac{3-f}{2}E_{\mathrm{r}}\mathbf{u}\right) - \lambda\mathbf{u}\cdot\nabla E_{\mathrm{r}} = c\kappa_{\mathrm{P}}\left(aT^4 - E_{\mathrm{r}}^{(0)}\right) + \nabla\left(\frac{c\lambda}{\chi_{\mathrm{R}}}\nabla E_{\mathrm{R}}\right)\,, \tag{4.19}$$

where ρ, $\mathbf{u}$, p, T, and E are the mass density, velocity, pressure, temperature, and total energy per unit mass. The a is equal to $a = \frac{4\sigma}{c}$, where σ is Stefan-Boltzmann constant. The κ_{P} is Planck mean interaction coefficients and f is Eddington factor, which is equal to $f = \lambda + \lambda^2 R^2$ and approach 0 and 1.

4.3.4 Input parameters and other characteristics

Geometry and boundaries

CASTRO offers two types of geometries. Cartesian (x, y, z) for all dimensions simulations, cylindrical (x, z) for 2D and spherical (r) for 1D simulations only. For the simulations in this thesis, the cylindrical geometry was chosen. Boundaries were set from $[0,0]$ to $[1.7375, 1.7375] \times 10^{16}$ cm with the center in $[0,0]$ and non-periodic boundaries because only a quarter of the domain was plotted. The boundary conditions selected were slipwall for each low face to mirror and simulate the domain as closely as possible and outflow for each high face with free boundary conditions for values of quantities.

Physics

The EOS used was the gamma-law (with $\gamma = \frac{5}{3}$) as mentioned in section 4.3.2. The radiation for a specific example was the Gray Radiation Hydrodynamic, described in

more detail in section 4.3.3. The Neumann boundary condition was applied to radiation. This boundary condition defines the values of the derivative at the domain boundaries. From Physics, Reactions, Sponge, and Gravity (due to its low influence) were disabled. Limiting the maximum velocity ($v = 1 \times 10^{11}$ cm s^{-1}) will prevent extreme values of quantities and slow down the calculation.

Other characteristics

The Courant number, which affects the speed of calculations, was set to $C = \frac{2}{3}$. One time step was 3×10^5 s, allowing data from more than 2,000 moments to be obtained. Usually, the simulation was stopped earlier when the matter from the supernova reached the boundaries.

4.4 SEDONA

SEDONA is a Monte Carlo radiative transfer code developed by Kasen et al. (2006) to address the three-dimensional time-dependent radiative transfer problem in rapidly expanding supernova atmospheres. It is designed to compute the light curves, spectra, and polarisation of aspherical supernova models providing a detailed treatment of the gamma-ray transfer from radioactive decay and a radiative equilibrium solution of the temperature structure. SEDONA furnishes a direct link between multi-dimensional hydrodynamic explosion models and observations, without the need to adjust free parameters in the radiative transfer calculation.

4.4.1 The structure of the iteration of the transfer code

At the outset, it is necessary to disclose the significant physical approximations utilized by the code:

- **Homologous expansion**, where the SN ejecta is assumed to be a free expansion with a homologous velocity structure, so that the velocity field of the ejecta is always spherically symmetric, even if the density structure of the ejecta is not.
- The **Sobolev approximation** delivers a straightforward and elegant method for solving line transfer for atmospheres with large gradients such as SNe.
- The **Equilibrium assumptions** deem that the ionization/excitation state of the SN gas follows local thermodynamic equilibrium (LTE) and can be calculated using the Saha ionization and Boltzmann excitation equations.

1. 3D gamma-ray transfer routine

This step determines the energy deposition rate in each cell from the decay of ^{56}Ni and ^{56}Co. Together with any initial shock-deposited energy, it operates as the source geometry for the optical photon packets.

2. Calculation of Opacities and Emissivities

Opacities and Emissivities are determined at all wavelengths for each cell and at each time step. Since the cell temperatures at each time are not initially known, a reasonable guess is made and refined iteratively.

The total absorptive opacity from all sources is their total sum

$$\alpha_{\text{abs}} = \alpha_{\text{abs, line}} + \alpha_{\text{abs, exp}} + \alpha_{\text{bf}} + \alpha_{\text{ff}} \,. \tag{4.20}$$

Here, the free-free opacity α_{ff} is calculated using standard formulas, and the bound free (photoionization) opacity α_{bf} is taken from the Opacity Project. The remaining two opacities are figured in this code. The absorptive component of the line expansion opacity is defined as

$$\alpha_{\text{abs, exp}}(\lambda) = \frac{1}{ct_{\text{exp}}} \sum_i \frac{\lambda_i}{\Delta\lambda_c} \frac{\epsilon}{\beta + \epsilon(1-\beta)} \left(1 - e^{-\tau_i}\right) \,. \tag{4.21}$$

The c is the speed of light and the time since the explosion is expressed as t_{exp}. The λ_c is the central wavelength of the bin and the sum operates over all the lines in the bin of width $\Delta\lambda_c$. The probability of absorption and the escape probability are represented by ϵ and β, respectively. The final quantity is the Sobolev line optical depth τ, which is based on the Sobolev approximation.

The purely absorptive component of the opacity from the lines treated directly $\alpha_{\text{abs, line}}$ is determined as

$$\alpha_{\text{abs, line}} = \frac{1}{ct_{\text{exp}}} \sum_i \frac{\lambda_i}{\Delta\lambda_c} p_{\text{abs}} \left(1 - e^{-\tau_i}\right) \,, \tag{4.22}$$

where the only previously undescribed variable is the probability of the photon being absorbed in the transition p_{abs}. The probability of true absorption is encountered to be very low for the conditions in SN atmospheres, $p_{\text{abs}} \approx 10^{-6} - 10^{-4}$.

3. Propagation of Photon Packets

The propagation of optical photon packets through space and time is tracked, providing a suitable summation of the photon absorption rate in each cell. The optical photon packets used in the Monte Carlo simulation are monochromatic and of equal energy.

Each packet has an initial energy E_p and describes a collection of $N_\mathrm{p} = \frac{E_\mathrm{p}\lambda}{hc}$ photons of a wavelength λ. Throughout any absorption/scattering interaction, the comoving frame energy of the packet is locked, even though the event changes the packet wavelength.

A velocity step corresponds to a physical distance in the ejecta, and photon packets are propagated through space and time until they reach the outer edge of the spatial grid, where they are considered to be observed.

4. Calculation of Temperature Structure

For each point on the space-time grid, the temperature calculation involves balancing the thermal emission rate with the photon absorption rates, as well as accounting for any radioactive energy deposition. This process is crucial in determining the opacities and emissivities of the gas.

As the new temperature differs from the one used to calculate the opacities, it is necessary to go back to step 2 and start again. This iterative process continues until the changes in quantities become insignificant.

5. Synthetic light curves and flux spectra

The resulting synthetic light curve and spectra are obtained after the convergence of the atmospheric model by collecting all the photon packets that have escaped from the atmosphere along a given line of sight.

The bolometric luminosity for the time series of the light curve at the frequencies and output times is calculated as follows

$$L_\mathrm{bol}(\{t\}) = \int_{\{\nu\}} L_{\{\nu\}}(\{t\})\,\mathrm{d}\nu\,, \tag{4.23}$$

and absolute bolometric magnitude is equal to

$$M_\mathrm{bol} = -2.5\log_{10} L_\mathrm{bol} + 88.697425\,. \tag{4.24}$$

4.4.2 Input data and parameters

Input models

For the input model, Sedona has a Python script that can generate a model in 1D, 2D and 3D based on user-specified quantities such as progenitor mass, maximum velocity limit, explosion time, atomic and mass number, number of cells, bounds and lower bounds for density and temperature. The models for calculating light curves and optical spectra in this thesis were based on models from CASTRO. The data from CASTRO

were transferred using the Python script, based on the SEDONA Python script for models, written by Petr Kurfürst. Only the grid over which the calculation was performed was more diluted. Compared to CASTRO, where the number of cells was 3600, the number of cells was adjusted to 360, i.e. every tenth value was taken. A second quarter was also fed into the model from CASTRO, where only one quarter was modeled in CASTRO and therefore symmetry was used to get SEDONA to calculate correctly. Therefore, the range of cells used was 360 (r-axis) $\times$ 720 (z-axis).

Geometry

As the Sedona can operate in up to three dimensions, it is necessary to set the grid geometry. The 1D mode uses spherical coordinates (r), the 2D mode uses cylindrical coordinates (r, z) and the 3D mode uses cartesian (x, y, z) or spherical coordinates (r, θ, φ). For the models in this thesis, cylindrical coordinates are utilized because the model from CASTRO is 2D.

Another parameter (*spectrum_n_mu*) related to geometry can determine the domain's division on sections with similar polar angles. For the models in this thesis, the domain was divided into 12 parts from $-\frac{\pi}{2}$ to $\frac{\pi}{2}$.

Radiation transport and sources

These parameters offer many possibilities to influence the radiation, starting with the number of particles initializing the simulation, which was set to $N = 10^7$. If there is a shortage of particles at some points during the last iteration, they can be replenished using the so-called last iteration pump.

Boundaries were also set for the frequency used for opacity and transport calculations $(10^{14}, 8 \times 10^{15})\,\mathrm{s}^{-1}$ with the step $\nu = 5 \times 10^{12}\,\mathrm{s}^{-1}$. Frequencies are recalculated to wavelengths.

The value of the gray opacity was determined to be $\alpha_{\mathrm{nu}} = 0.34\,\mathrm{cm}^2\,\mathrm{g}^{-1}$, other opacities were gained by the procedure described in the section 4.4.1 (Kassen, 2018).

Once all the parameters have been set and the model has been prepared, the desired synthetic light curve and spectrum can be calculated.

Chapter 5

Models

The star chosen for this work is a hydrogen-rich RSG with mass $M_* = 15\,M_\odot$ and radius $R_* = 7.285 \times 10^{13}$ cm (approximately $R_* = 1050\,R_\odot$), surrounded by an equatorial disk and a bipolar nebula.

The working procedure followed the same order as sections in Chapter 4. Firstly, a model was created for this star in SNEC that was supplemented with the CSM modeling code to add the disk and lobes. This model has been inputted into CASTRO, which can work with data from SNEC. After the calculation in CASTRO, the data were converted into supported formats and reformatted into the SEDONA-supported form. After all the procedures in SEDONA, the light curve and spectra were obtained.

5.1 SNEC

From the SNEC simulation the temperature and density at the time just after the shock breakout and the end of the simulation were selected. The temperature distribution in the model shows significant differences in the various phases of the supernova explosion, and the same can be set for the density.

After the shock breakout, two main groups can be seen in both plots (5.1a, 5.2a). The first one, with a lower density and temperature, located between $0.2\,R_*$ and $0.4\,R_*$, is probably the remnant of the core. The higher peaks illustrate the matter transferred into the hot photosphere.

Figures 5.1b and 5.2b show the temperature and density distributions at the end of the simulation, 195 days after the shock breakout. Most of the matter from supernovae remains in the region up to $50\,R_*$, which could be called the supernova remnant.

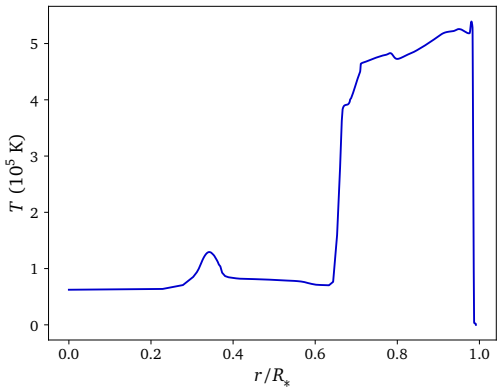

(a) Temperature distribution graph immediately after a shock breakout.

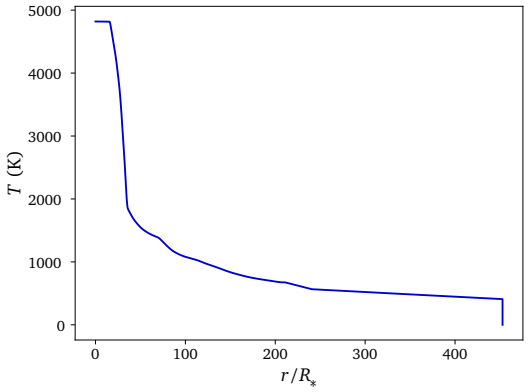

(b) Temperature distribution graph 195 days after a shock breakout.

Figure 5.1: Temperature distribution graphs from SNEC for situations immediately after a shock breakout and 195 days after.

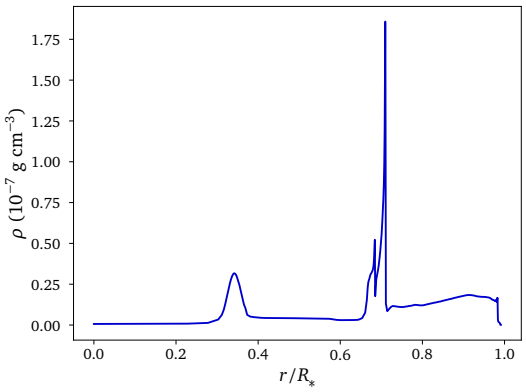

(a) Density distribution graph immediately after a shock breakout.

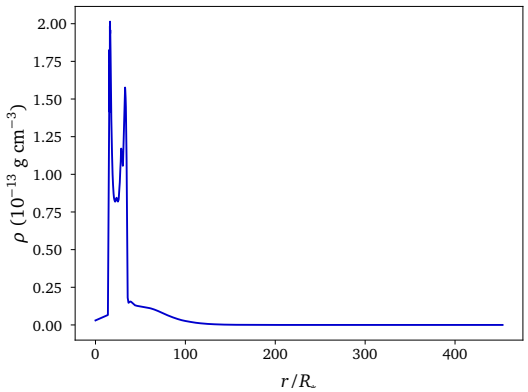

(b) Density distribution graph 195 days after a shock breakout.

Figure 5.2: Density distribution graphs from SNEC for situations immediately after a shock breakout and 195 days after.

5.2 Models of interactions

Models of supernova evolution interacting with the CSM were created in CASTRO, using SNEC data at the time of shock breakout as input but enriched by the CSM. Graphs were then created for the 4 quantities at different times, showing their evolution. For density and temperature, more general times were chosen, at the beginning of the simulation, in the middle, and at the end. Similarly, the radial energy and velocity for the SN with disk, for which only the first plot at time t = 50 d was changed since these quantities are initially zero. Depending on the deceleration of the ejecta by lobes, three times were selected for the velocity distribution in SN with lobes.

Figures 5.3a and 5.3b show the density distribution at the origin and therefore the composition of the added CSM. The temperature in figures 5.5a and 5.5b also refers to the initial state, where it can be seen that all the surroundings are cool except for the progenitor. The velocity figures 5.4 show the difference in composition between the disk and lobes. The ejecta is only slowed down by lobes at a time approximately $t = 115$d (5.4a), $t = 278$d (5.4c), and $t = 415$d (5.4e). The disk with a higher density than lobes is more difficult for ejecta to penetrate and is significantly slowed down. The difference between the two environments, where the ejecta propagates freely in one and much more slowly in the other, leads to Kelvin-Helmholtz instabilities (vortex).

Thin layers, called overdensities, can form at points where shocked gas is pushed into place with higher density (CSM) and then is pushed above and below. This very thin overdensity can be seen in Figure 5.3d.

For all temperature plots, the highest temperature is always concentrated at the location of the expanding stellar remnant. In the case of the disk, the situation is more interesting, where the last plot shows how slowly the ejecta penetrates the disk and thus the temperature is accumulated in addition to the density.

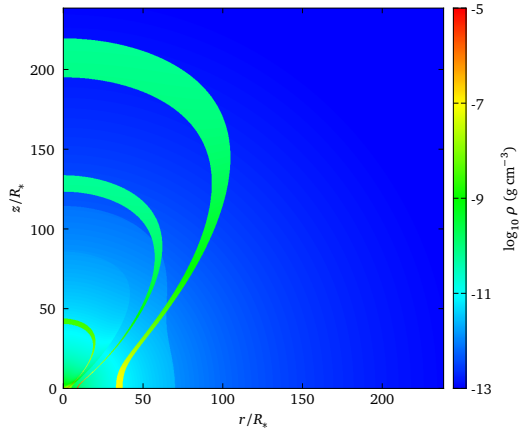

(a) SN explosion with lobes at $t = 0$ d.

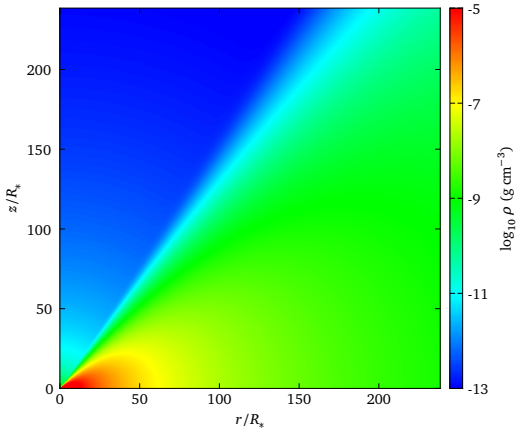

(b) SN explosion with disk at $t = 0$ d.

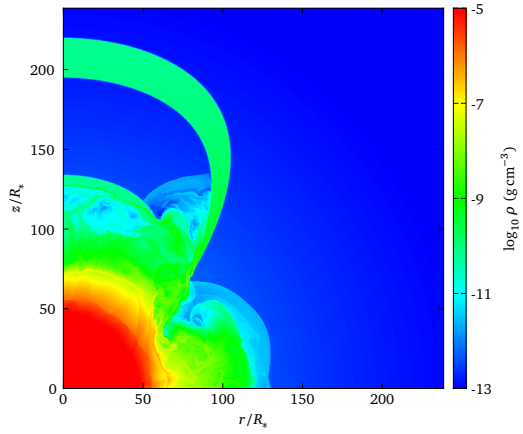

(c) SN explosion with lobes at $t = 288$ d.

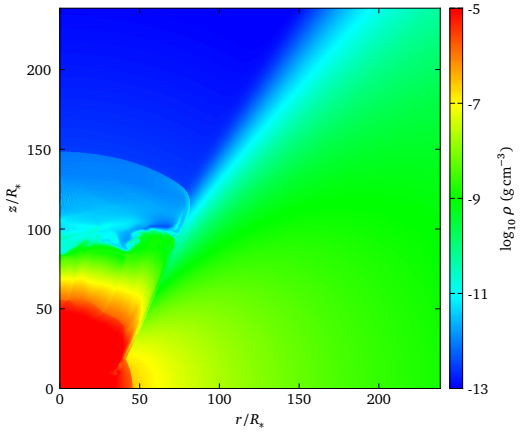

(d) SN explosion with disk at $t = 288$ d.

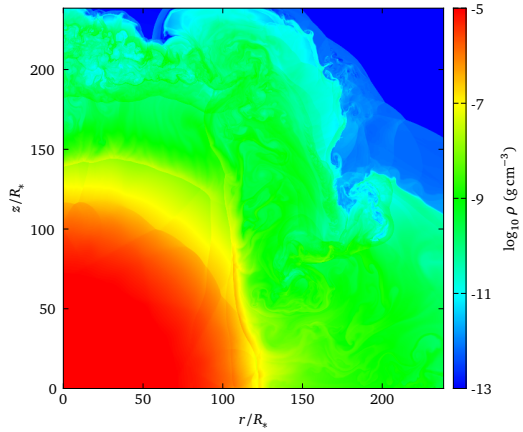

(e) SN explosion with lobes at $t = 580$ d.

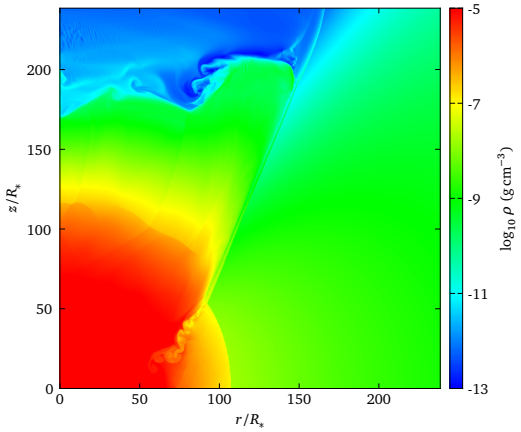

(f) SN explosion with disk at $t = 580$ d.

Figure 5.3: Density distribution graphs.

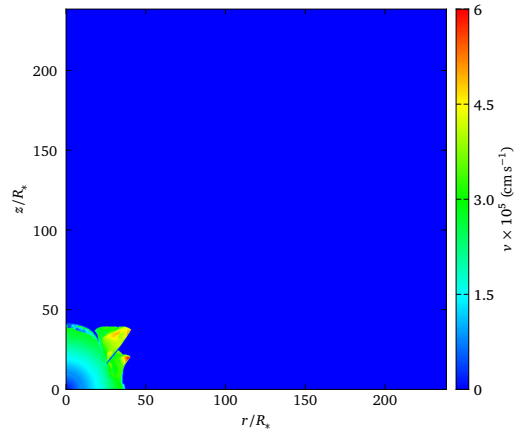

(a) SN explosion with lobes at $t = 115$ d.

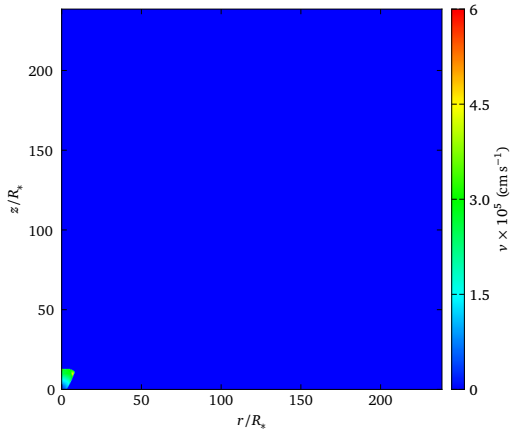

(b) SN explosion with disk at $t = 35$ d.

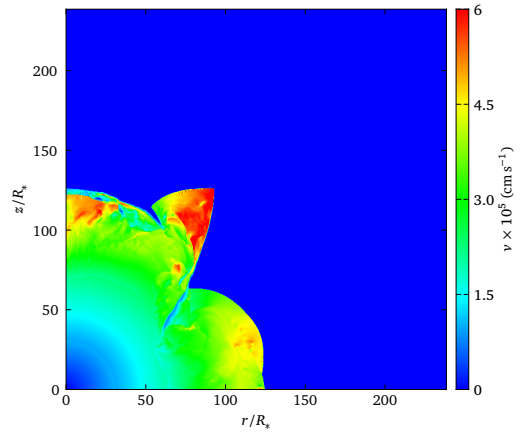

(c) SN explosion with lobes at $t = 278$ d.

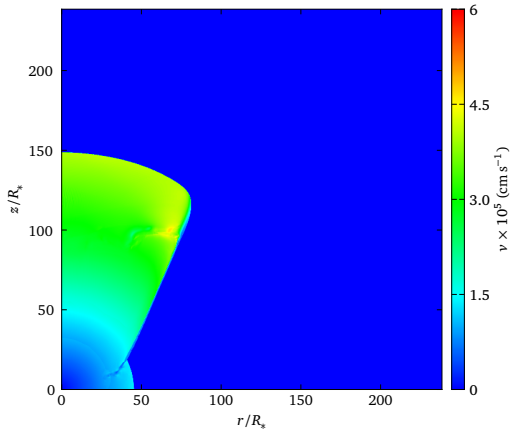

(d) SN explosion with disk at $t = 288$ d.

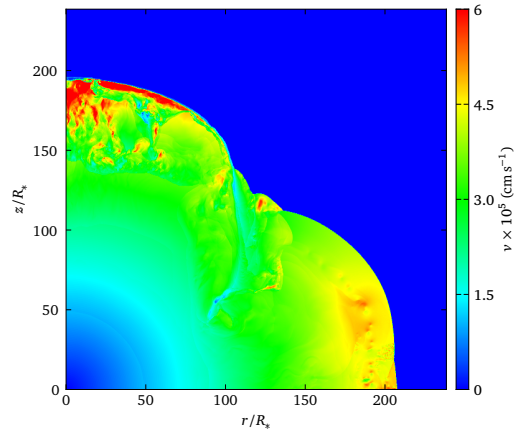

(e) SN explosion with lobes at $t = 413$ d.

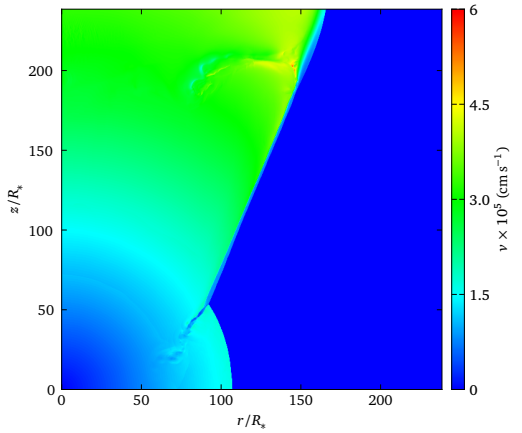

(f) SN explosion with disk at $t = 580$ d.

Figure 5.4: Velocity distribution graphs.

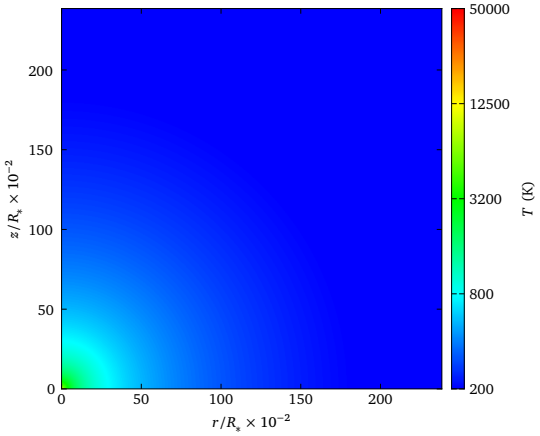

(a) SN explosion with lobes at $t = 0$ d.

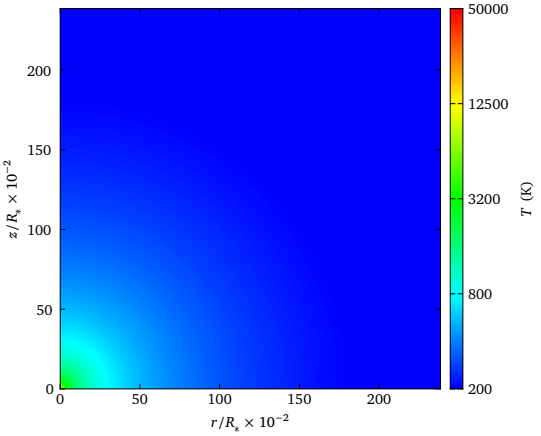

(b) SN explosion with disk at $t = 0$ d.

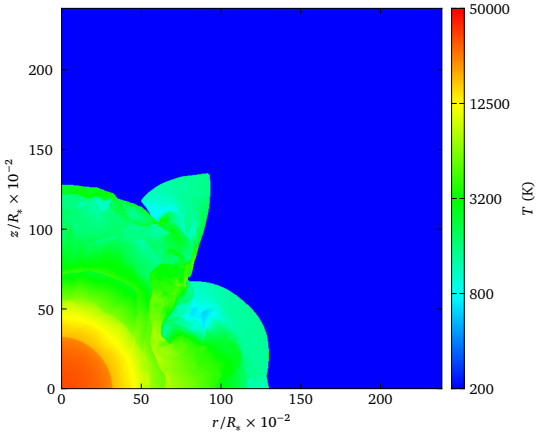

(c) SN explosion with lobes at $t = 288$ d.

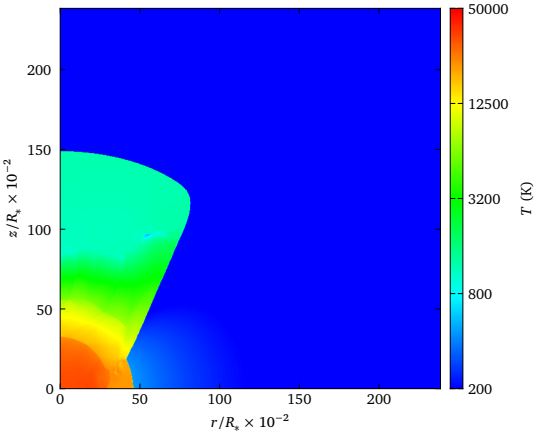

(d) SN explosion with disk at $t = 288$ d.

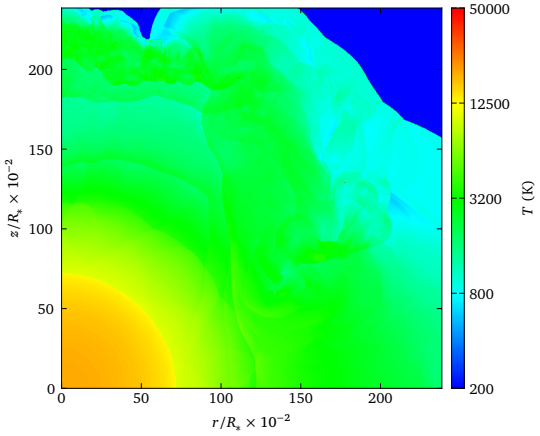

(e) SN explosion with lobes at $t = 580$ d.

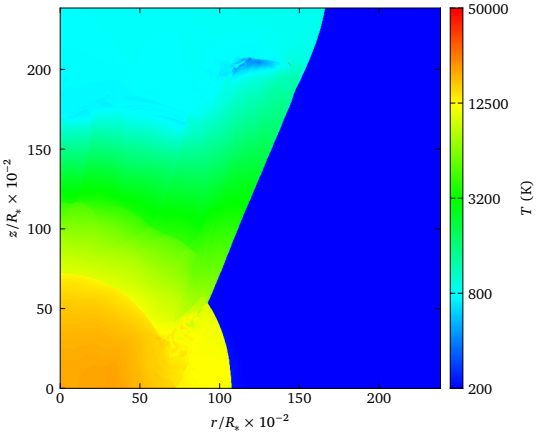

(f) SN explosion with disk at $t = 580$ d.

Figure 5.5: Temperature distribution graphs.

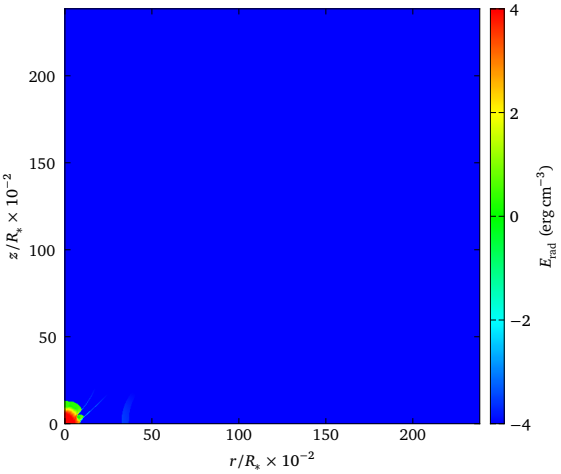

(a) SN explosion with lobes at $t = 35$ d.

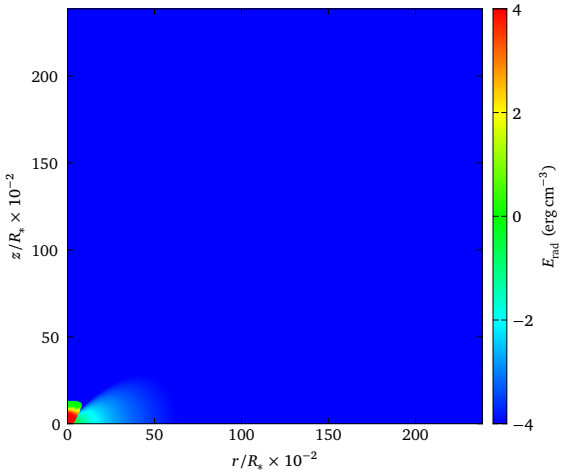

(b) SN explosion with disk at $t = 35$ d.

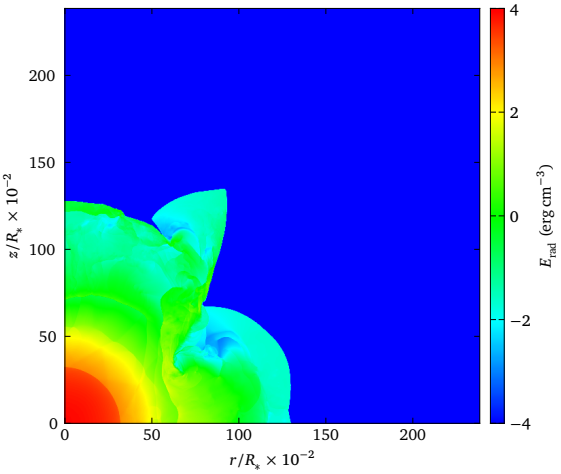

(c) SN explosion with lobes at $t = 288$ d.

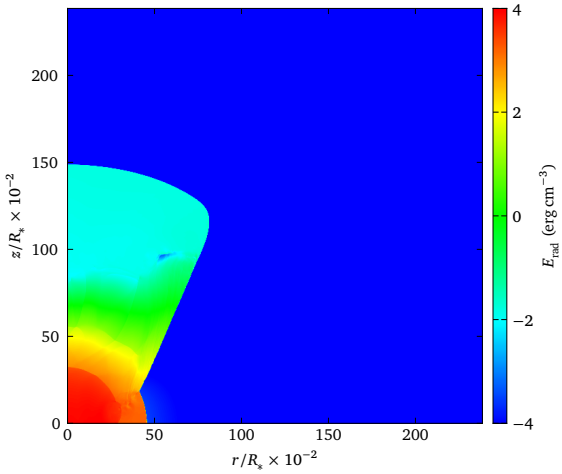

(d) SN explosion with disk at $t = 288$ d.

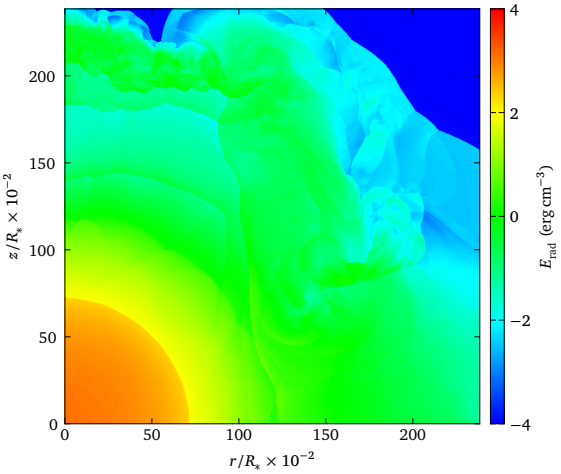

(e) SN explosion with lobes at $t = 580$ d.

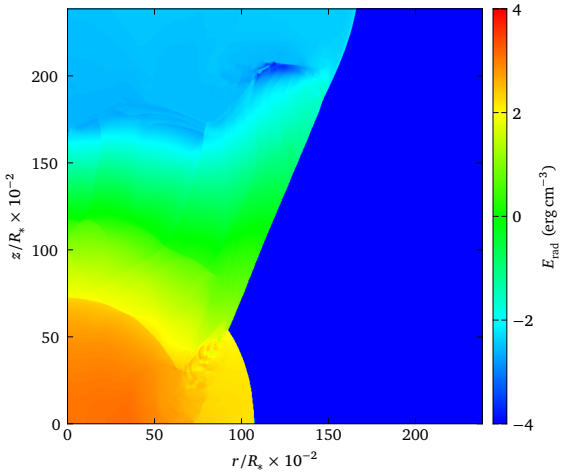

(f) SN explosion with disk at $t = 580$ d.

Figure 5.6: Radiative energy distribution graphs.

5.3 Light curves

Synthetic light curves were obtained from SEDONA as a result of postprocessing data from CASTRO with the same time step ($t_{\text{step}} = 3.48$ d). They were then compared to the SN without interactions with CSM but powered by $0.28 M_{\odot}$ radioactive nickel. The resulting luminosity from SEDONA should be bolometric, but in this case, it was only quasi-bolometric because the full range of frequencies was not used. Light curves based on CSM interaction events have a longer rise time to the maximum, but it is approximately one order of magnitude higher in quasi-bolometric luminosity. The absolute quasi bolometric magnitude can be calculated from equation 2.2 and the knowledge of the peak luminosity ($L_{\text{bol, lobes}} = 3.57 \times 10^{43}\,\text{erg}\,\text{s}^{-1}$ and $L_{\text{bol, disk}} = 1.83 \times 10^{43}\,\text{erg}\,\text{s}^{-1}$). For SN with bipolar lobes (5.7) is the absolute quasi-bolometric magnitude $M_{\text{bol, lobes}} = -20.19$ mag and for SN with equatorial disk (5.8) $M_{\text{bol, disk}} = -19.46$ mag. In the light curve of the supernova interacting with the bipolar lobes, a version of the late bump occurs around $t = 150$ d.

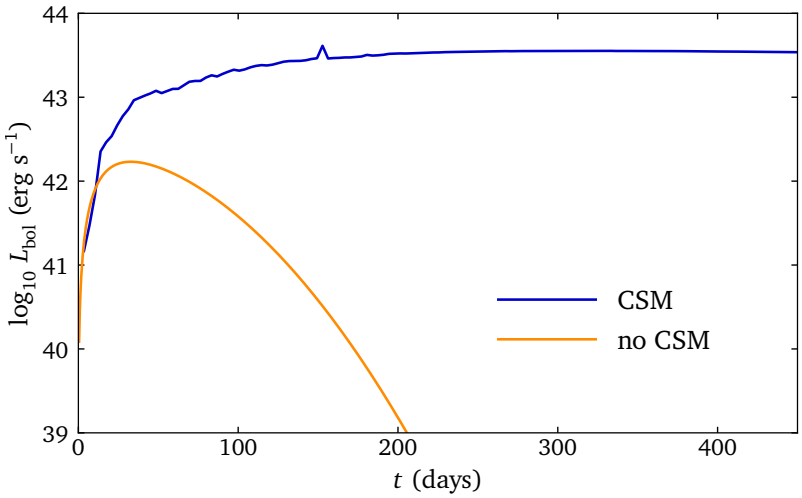

Figure 5.7: Graph comparing synthetic light curves with CSM and without CSM. The blue line (CSM) represents SN interacting with bipolar lobes. The orange line (no CSM) refers to SN powered by radioactive nickel.

5.4 Spectra

Spectra were also calculated from SEDONA including the electron scattering boun-bound, bound-free, and free-free opacity. The Doppler broadening of spectral lines was also included and set in the range of $\pm 10{,}000$ km s^{-1}. SEDONA produced a spectral continuum with jumps (Balmer jumps) and also showed the profiles of the Balmer lines (only hydrogen was included in the chemical structure of the supernova and the CSM). On the left of the Balmer jump which occurres at about 4000 Å, within shorter

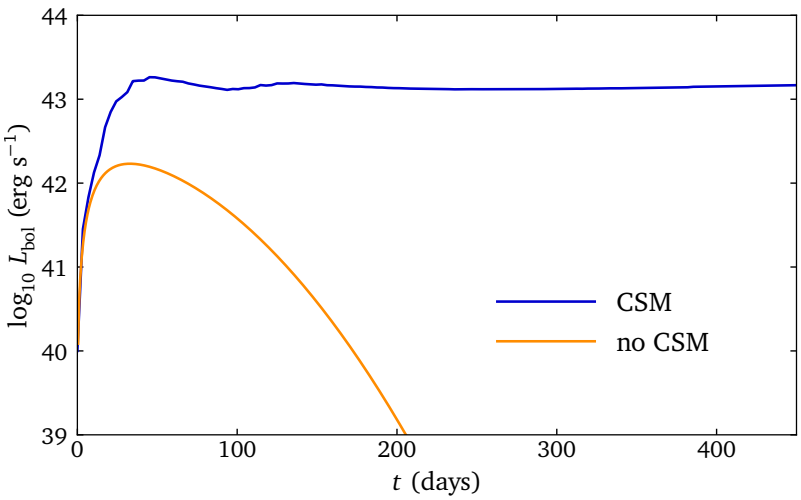

Figure 5.8: Graph comparing synthetic light curves with CSM and without CSM. The blue line (CSM) represents SN interacting with the equatorial disk. The orange line (no CSM) refers to SN that is powered by radioactive nickel.

wavelengths, the Lyman lines are well documented. Spectra are from the pole view ($\theta \approx 0$) and in the from 200 Å to 29,600 Å. Graphs 5.9 and 5.10 show spectra for three situations after a shock breakout (bo) - 25 days, 100 days, and 400 days after. The most important lines in hydrogen-rich SNe are the hydrogen, especially Hα (6560 Å) and Hβ (4860 Å) lines, both of which are indicated in the graphs. The flux values in the spectra are scaled relative to each other for comparison (relative flux).

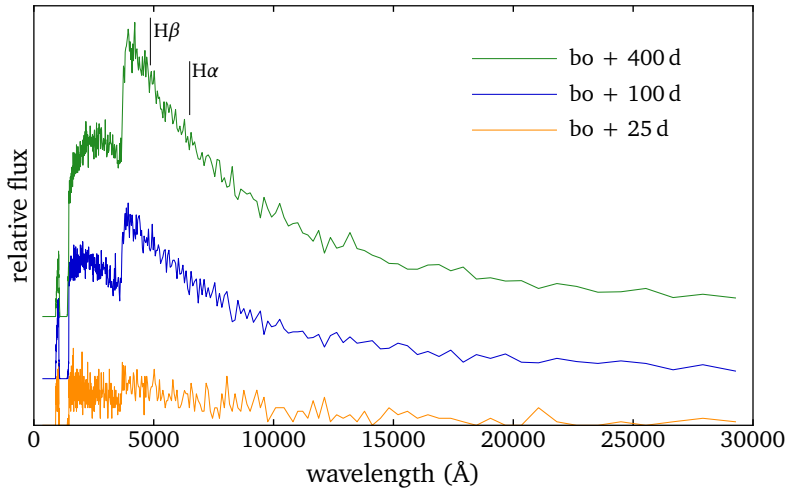

Figure 5.9: Graph comparing synthetic spectra at three situations after shock breakout (bo) for SN interacting with lobes.

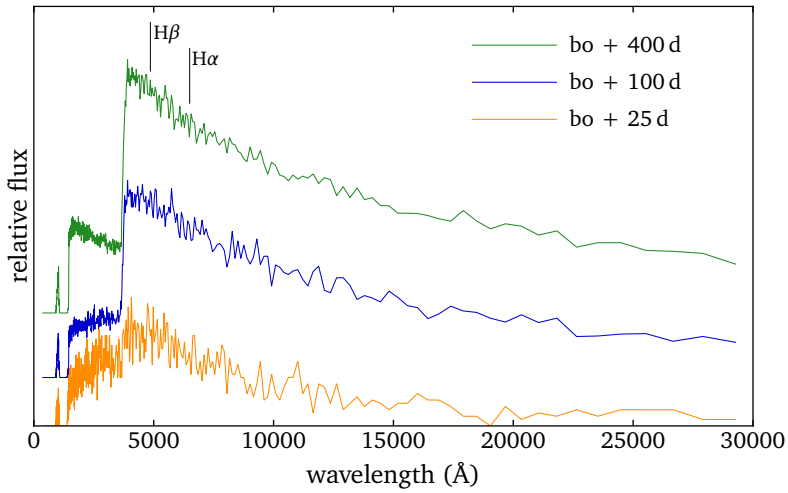

Figure 5.10: Graph comparing synthetic spectra at three situations after shock breakout (bo) for SN interacting with disk.

5.5 Discussion

The quantities estimated from calculations in this thesis in the case of both simulations agree in principle with what was presented, e.g., in Kurfürst et al. (2020); Kurfürst & Krtička (2019); McDowell et al. (2018), and also with what was observed. The hydrodynamical structure in the models demonstrates the expected evolution of the matter that expands much faster in the polar direction in the SN-disk model while it is basically hampered in the equatorial direction. This effect is caused by the interaction with a much denser disk environment. The corresponding evolution in the velocity and temperature structure goes hand-in-hand. However, even the pole-on velocity is lower than in Kurfürst et al. (2020) or Kurfürst & Krtička (2019) models, which is caused by the implementation of the radiation-cooling process in the current simulations (while the previous hydrodynamic models were purely adiabatic). The evolution of the overdensity and instability strips is also similar to previous referred models. A comparable situation occurs in the bipolar lobes models. Here, the density, velocity, and temperature structure form a mostly pole-on-evolving expansion with numerous irregularities and instabilities caused by the hindering interaction with the denser shells of the polar lobes in the previously formed circumstellar medium. The velocity field is in this model also significantly variable, in dependence on the density structure in the particular direction of expansion.

The particular problem and therefore the essential future task is the proper calibration of the initial mass of the surrounding CSM structures. This affects the interaction shock power which is then projected into the intensity and the duration of the light curves. In the current models, this initial mass/density structure is somewhat roughly determined, so it may give rather high values in comparison with the actually observed light curves. However, apart from this calibration, the evolutionary structure

of the light curves shows a pretty consistent profile with the light curves calculated in the models from Kurfürst et al. (2020); Kurfürst & Krtička (2019). For example, the luminosity bump near 150 days in the SN-lobes interaction light curve resembles a similar bump in the corresponding light curve in Kurfürst et al. (2020). The slight early-on shift here is caused by the smaller size of the whole model. On the other hand, the light curves (particularly the SN-lobes interaction light curve) show less dramatic evolution than those in Kurfürst et al. (2020). It is likely due to the hydrodynamically smoother density-velocity-temperature evolution caused by the radiation processes implementation into the CASTRO models. However, the latter will be the principal focus of further detailed research and modeling.

The spectra calculated at different times for both models are merely an illustrative sample of the spectral evolution. They do not contain particular details of spectral lines evolution, even though they are calculated by the inclusion of the Doppler broadening of spectral lines in the range of $\pm 10{,}000\,\mathrm{km\,s^{-1}}$. Since the SEDONA code spectra calculations involve the electron scattering, bound-bound, bound-free, and free-free opacities, the spectral profiles show except the typical jumps in the continuum (mainly the Balmer jump) also the Lyman lines between approximately $1550 - 3500$ Å. They indicate the Balmer lines in the region close above the Balmer jump. In the future, it will be important to calculate the spectral samples of typical Balmer lines in detail and compare the pattern of its broadening not only at different times but also from different viewing angles which is the main advantage of the used multidimensional SEDONA code.

As a matter of a future extension of the current work, it will be essentially interesting and important to introduce principally similar models of SN-aspherical CSM interaction where the CSM is not axially symmetric. For example, the study of the "interaction picture" of supernovae that exploded toward the central galactic disk on one side of the supernova progenitor, such as between the supernova and the observer (see, e.g., Moranchel-Basurto et al., 2021). This will show yet more aspherical patterns manifested mainly in the spectral lines broadening asymmetry, which gives more characteristic information about the density and spatial distribution of a pre-explosion CSM. This information could provide an invaluable source of knowledge about the stellar evolution just before and in the final stages of massive stars' "life".

An important task is also a proper comparison of the calculated models with observed events. Figure 5.11 shows a few light curves of prominent SLSNe adopted from (Kurfürst et al., 2020) where most of them, after an initial decrease, remain at approximately constant or even slightly increasing luminosity. The luminosity of SN iPTF14hls [3] in the early phase, up to around 200 days after the explosion, increases

[3]The labeling of the SNe refers to the intermediate Palomar Transient Factory (iPTF) observational campaign which was in operation in the years 2012 - 2018 and was later succeeded by the Zwicky Transient Factory (ZTF) and other more modern observational runs.

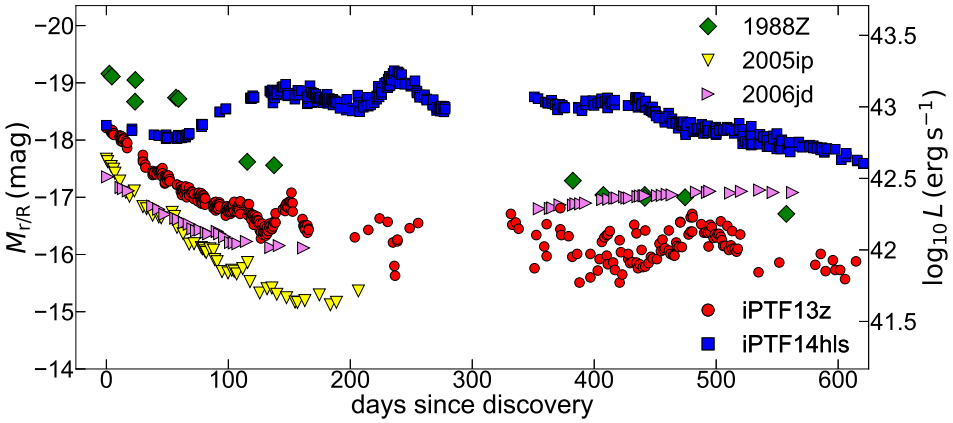

Figure 5.11: Light curves from several prominent observed SLSNe. Adopted from the paper *Supernova explosions interacting with aspherical circumstellar material: implications for light curves, spectral line profiles, and polarization* (Kurfürst et al., 2020).

and only then begins to slowly decrease. All of these light curves show several bumps or rebrightenings at a particular time which are likely caused by the variable environment within a sufficiently dense CSM. The models presented in this work are in a rather introductory phase of calculations using the combination of the CASTRO and SEDONA codes. The density/morphology structures of the CSM are currently only arbitrarily scaled, so the light curves of the models presented here show relatively higher luminosities than most of the observed events. This can be compensated by varying the parameters of the CSM in the future. The remaining task is to compare the calculated spectra with the observed ones. This is especially challenging for rotationally asymmetric CSMs such as one-sided disks or slabs of overdense pre-explosion structures, which are not presented here.

Conclusions

The topic of SNe is essential in all of astrophysics, especially for understanding the explosions of very massive stars, which significantly affect the evolution of the Universe. These are the crucial cosmic events responsible for the production and distribution of many chemical elements in the environment, which are the building blocks for the formation of new generations of stars and, on a global scale, influence the evolution of entire galaxies. In the faraway past, in the era of the First Stars in the Universe (stars of Population III), these extremely massive stars ended their lives almost entirely as core-collapse SNe, enriching the Universe mainly with metals, i.e. elements heavier than helium. They are also the most abundant sources of cosmic dust, the particulate matter that is a critical ingredient in the formation of planets and potentially the conditions for life. Last but not least, supernovae are producers of compact objects such as neutron stars or black holes. Objects that, apart from being utterly interesting and fascinating, are also the sources of other phenomena that have been studied only recently and are therefore of timely interest, like gamma-ray bursts and gravitational wave events. All of these topics form together a relatively new and exceptionally challenging field of investigation within the whole of astrophysics.

After an SN explosion, the expanding mass interacts at speeds in the order of $10,000\ \mathrm{km\,s^{-1}}$ with the surrounding environment, throwing the surrounding material in front of it, which heats up very strongly. This is the reason why it is possible to observe such interactions. For some SNe, these interactions with the surrounding material become a dominant factor in their light curves and spectra, providing a valuable tool for tracing the structure, density, and shape of the surrounding material over large distances. It also allows astrophysicists to estimate the evolutionary history of stars and even larger objects such as star clusters or entire galaxies.

The main aim of this thesis was to study this phenomenon theoretically, using numerical simulations, and to compare in principle the models with actually observed events of a similar nature up to about 450 days after the SN explosion. In the theoretical part, this phenomenon, along with the associated processes closely related to the origin, is explained in detail, as well as the consequences of these explosions. The models of supernovae interacting with the surroundings were calculated in the practical part. The two types of interactions with two CSM morphologies that were previously

formed in the vicinity of the progenitor star have been simulated, a dense equatorial disk and the bipolar lobes. The models include quantities such as density, expansion velocity, and last but not least temperature. Based on the hydrodynamic models, light curves of both the interactions and theoretical spectra at various times of the process have been calculated. A simple comparison with real observables of a few prominent events of a similar type is also introduced. Both goals, which were introducing the topic of supernovae and making models, have been successfully achieved. It is noticeable that the numerical models of SNe interacting with their surroundings are rather simplified to illustrate the explosion itself and the subsequent expansion of matter into the surroundings. The results can thus be regarded as the important practical basis for further studies in this field of research.

Bibliography

A. S. Almgren, V. E. Beckner, J. B. Bell, M. S. Day, L. H. Howell, C. C. Joggerst, M. J. Lijewski, A. Nonaka, M. Singer, & M. Zingale. Castro: A new compressible astrophysical solver. i. hydrodynamics and self-gravity. *The Astrophysical Journal*, 715(2):1221, may 2010. doi: 10.1088/0004-637X/715/2/1221. URL `https://dx.doi.org/10.1088/0004-637X/715/2/1221`.

A. W. Alsabti & P. Murdin. Supernovae and Supernova Remnants: The Big Picture in Low Resolution. In A. W. Alsabti & P. Murdin, editors, *Handbook of Supernovae*, page 3. Springer, 2017. doi: 10.1007/978-3-319-21846-5_1.

I. Arcavi. Hydrogen-Rich Core-Collapse Supernovae. In A. W. Alsabti & P. Murdin, editors, *Handbook of Supernovae*, page 239. Springer, 2017. doi: 10.1007/978-3-319-21846-5_39.

R. Barbon, F. Ciatti, & L. Rosino. Photometric properties of type II supernovae. *Astronomy & Astrophysics*, 72:287–292, Feb. 1979.

D. S. Birney, G. Gonzalez, & D. Oesper. *Observational Astronomy*. Cambridge University Press, 2 edition, 2006.

D. Branch. Spectra of supernovae. In *Supernovae*, pages 30–58, Jan. 1990.

D. Branch & J. C. Wheeler. *Supernova Explosions*. Springer, 2017. doi: 10.1007/978-3-662-55054-0.

B. W. Carroll & D. A. Ostlie. *An Introduction to Modern Astrophysics*. Cambridge University Press, 2 edition, 2017.

J. S. W. Claeys, S. E. de Mink, O. R. Pols, J. J. Eldridge, & M. Baes. Binary progenitor models of type IIb supernovae. *Astronomy & Astrophysics*, 528:A131, Apr. 2011. doi: 10.1051/0004-6361/201015410.

L. Dessart, S.-C. Yoon, D. R. Aguilera-Dena, & N. Langer. Supernovae Ib and Ic from the explosion of helium stars. *Astronomy & Astrophysics*, 642:A106, Oct. 2020. doi: 10.1051/0004-6361/202038763.

J. Dexter & D. Kasen. Supernova Light Curves Powered by Fallback Accretion. *The Astrophysical Journal*, 772(1):30, July 2013. doi: 10.1088/0004-637X/772/1/30.

J. B. Doggett & D. Branch. A comparative study of supernova light curves. *Astronomical Journal*, 90:2303–2311, Nov. 1985. doi: 10.1086/113934.

M. R. Drout, A. M. Soderberg, A. Gal-Yam, S. B. Cenko, D. B. Fox, D. C. Leonard, D. J. Sand, D.-S. Moon, I. Arcavi, & Y. Green. The First Systematic Study of Type Ibc Supernova Multi-band Light Curves. *The Astrophysical Journal*, 741(2):97, Nov. 2011. doi: 10.1088/0004-637X/741/2/97.

A. V. Filippenko. Optical Spectra of Supernovae. *Annual Review of Astronomy and Astrophysics*, 35:309–355, Jan. 1997. doi: 10.1146/annurev.astro.35.1.309.

A. Gal-Yam. Luminous Supernovae. *Science*, 337(6097):927, Aug. 2012. doi: 10.1126/science.1203601.

A. Gal-Yam. Observational and Physical Classification of Supernovae. In A. W. Alsabti & P. Murdin, editors, *Handbook of Supernovae*, page 195. Springer, 2017. doi: 10.1007/978-3-319-21846-5_35.

A. Gal-Yam. The Most Luminous Supernovae. *Annual Review of Astronomy and Astrophysics*, 57:305–333, Aug. 2019. doi: 10.1146/annurev-astro-081817-051819.

E. E. E. Gall, J. Polshaw, R. Kotak, A. Jerkstrand, B. Leibundgut, D. Rabinowitz, J. Sollerman, M. Sullivan, S. J. Smartt, J. P. Anderson, S. Benetti, C. Baltay, U. Feindt, M. Fraser, S. González-Gaitán, C. Inserra, K. Maguire, R. McKinnon, S. Valenti, & D. Young. A comparative study of Type II-P and II-L supernova rise times as exemplified by the case of LSQ13cuw. *Astronomy & Astrophysics*, 582:A3, Oct. 2015. doi: 10.1051/0004-6361/201525868.

D. Kasen, R. C. Thomas, & P. Nugent. Time-dependent Monte Carlo Radiative Transfer Calculations for Three-dimensional Supernova Spectra, Light Curves, and Polarization. *The Astrophysical Journal*, 651(1):366–380, Nov. 2006. doi: 10.1086/506190.

D. Kassen. Sedona6 Users Guide. `https://dnkasen.github.io/sedona_documentation/index.html`, 2018. [Accessed 12-04-2024].

S. Katsuda. Supernova of 1006 (G327.6+14.6). In A. W. Alsabti & P. Murdin, editors, *Handbook of Supernovae*, page 63. Springer, 2017. doi: 10.1007/978-3-319-21846-5_45.

R. P. Kirshner. Supernova light curves. In *Supernovae*, pages 59–75, Jan. 1990.

P. Kurfürst & J. Krtička. Modeling of interactions between supernovae ejecta and aspherical circumstellar environments. *Astronomy & Astrophysics*, 625:A24, May 2019. doi: 10.1051/0004-6361/201833429.

P. Kurfürst, O. Pejcha, & J. Krtička. Supernova explosions interacting with aspherical circumstellar material: implications for light curves, spectral line profiles, and polarization. *Astronomy & Astrophysics*, 642:A214, Oct. 2020. doi: 10.1051/0004-6361/202039073.

P. Kurfürst. Astrofyzika supernov. Master thesis, Masaryk university, Faculty of Science, 2010. URL `https://is.muni.cz/th/vgeo7/`.

B. Leibundgut & N. B. Suntzeff. Optical Light Curves of Supernovae. In K. Weiler, editor, *Supernovae and Gamma-Ray Bursters*, volume 598, pages 77–90. Springer, 2003. doi: 10.1007/3-540-45863-8_6.

M. S. Longair. *High Energy Astrophysics*. Cambridge University Press, 2011.

A. T. McDowell, P. C. Duffell, & D. Kasen. Interaction of a Supernova with a Circumstellar Disk. *Astrophysical Journal*, 856(1):29, Mar. 2018. doi: 10.3847/1538-4357/aaa96e.

A. Moranchel-Basurto, F. J. Sánchez-Salcedo, R. O. Chametla, & P. F. Velázquez. Supernova Explosions in Accretion Disks in Active Galactic Nuclei: Three-dimensional Models. *Astrophysical Journal*, 906(1):15, Jan. 2021. doi: 10.3847/1538-4357/abca88.

V. Morozova, C. D. Ott, & A. L. Piro. SNEC: SuperNova Explosion Code. Astrophysics Source Code Library, record ascl:1505.033, May 2015a.

V. Morozova, A. L. Piro, M. Renzo, C. D. Ott, D. Clausen, S. M. Couch, J. Ellis, & L. F. Roberts. Light Curves of Core-collapse Supernovae with Substantial Mass Loss Using the New Open-source SuperNova Explosion Code (SNEC). *The Astrophysical Journal*, 814(1):63, Nov. 2015b. doi: 10.1088/0004-637X/814/1/63.

NASA Hubble Space Telescope. M1 — flickr.com. `https://www.flickr.com/photos/nasahubble/35971297530/`, 2017. [Accessed 12-04-2024].

NASA's Marshall Space Flight Center. SN 1006: Liberating Star Stuff — flickr.com. `https://www.flickr.com/photos/nasamarshall/35407642044`, 2017. [Accessed 12-04-2024].

NASA's Marshall Space Flight Center. A View of Tycho's Supernova Remnant — flickr.com. `https://www.flickr.com/photos/nasamarshall/48859734028/`, 2019. [Accessed 12-04-2024].

D. E. Osterbrock. Who Really Coined the Word Supernova? Who First Predicted Neutron Stars? In *American Astronomical Society Meeting Abstracts*, volume 199 of *American Astronomical Society Meeting Abstracts*, page 15.01, Dec. 2001.

B. Paxton, L. Bildsten, A. Dotter, F. Herwig, P. Lesaffre, & F. Timmes. Modules for Experiments in Stellar Astrophysics (MESA). *The Astrophysical Journal Supplement*, 192(1):3, Jan. 2011. doi: 10.1088/0067-0049/192/1/3.

S. Prajs. *Superluminous supernovae in large astronomical surveys*. PhD thesis, University of Southampton, March 2019. URL `https://eprints.soton.ac.uk/456253/`.

M. W. Richmond, R. R. Treffers, A. V. Filippenko, Y. Paik, B. Leibundgut, E. Schulman, & C. V. Cox. UBVRI Photometry of SN 1993J in M81: The First 120 Days. *Astronomical Journal*, 107:1022, Mar. 1994. doi: 10.1086/116915.

S. Rosswog & M. Brüggen. *Introduction to High-Energy Astrophysics*. Cambridge University Press, 2011.

G. N. Sabhahit, J. S. Vink, A. A. C. Sander, & E. R. Higgins. Very massive stars and pair-instability supernovae: mass-loss framework for low metallicity. *Monthly Notices of the Royal Astronomical Society*, 524(1):1529–1546, Sept. 2023. doi: 10.1093/mnras/stad1888.

S. Schulze, T. Krühler, G. Leloudas, J. Gorosabel, A. Mehner, J. Buchner, S. Kim, E. Ibar, R. Amorín, R. Herrero-Illana, J. P. Anderson, F. E. Bauer, L. Christensen, M. de Pasquale, A. de Ugarte Postigo, A. Gallazzi, J. Hjorth, N. Morrell, D. Malesani, M. Sparre, B. Stalder, A. A. Stark, C. C. Thöne, & J. C. Wheeler. Cosmic evolution and metal aversion in superluminous supernova host galaxies. *Monthly Notices of the Royal Astronomical Society*, 473(1):1258–1285, Jan. 2018. doi: 10.1093/mnras/stx2352.

L. I. Sedov. Propagation of strong shock waves. *Journal of Applied Mathematics and Mechanics*, 10:241–250, Jan. 1946.

N. Smith. Interacting Supernovae: Types IIn and Ibn. In A. W. Alsabti & P. Murdin, editors, *Handbook of Supernovae*, page 403. Springer, 2017. doi: 10.1007/978-3-319-21846-5_38.

V. Vanýsek. *Základy astronomie a astrofyziky*. Academia, Praha, 1980.